Petroleum Science 21 (2024) 1699–1718

Contents lists available at ScienceDirect

Petroleum Science

journal homepage: www.keaipublishing.com/en/journals/petroleum-science

Original Paper

Geostatistical seismic inversion and 3D modelling of metric flow units, porosity and permeability in Brazilian presalt reservoir

Rodrigo Penna [a, b, *], Wagner Moreira Lupinacci [a]

[a] Exploratory Interpretation and Reservoir Characterization Group (GIECAR), Department of Geology and Geophysics, Universidade Federal Fluminense, Niterói, RJ, 24210-346, Brazil
[b] Petrobras, Rio de Janeiro, RJ, 20031-912, Brazil

ARTICLE INFO

Article history:
Received 11 May 2022
Received in revised form
29 January 2024
Accepted 26 February 2024
Available online 27 February 2024

Edited by Jie Hao and Meng-Jiao Zhou

Keywords:
Flow units
Geostatistical inversion
Presalt reservoir
3D reservoir modelling
Petrophysical modelling

ABSTRACT

Flow units (FU) rock typing is a common technique for characterizing reservoir flow behavior, producing reliable porosity and permeability estimation even in complex geological settings. However, the lateral extrapolation of FU away from the well into the whole reservoir grid is commonly a difficult task and using the seismic data as constraints is rarely a subject of study. This paper proposes a workflow to generate numerous possible 3D volumes of flow units, porosity and permeability below the seismic resolution limit, respecting the available seismic data at larger scales. The methodology is used in the Mero Field, a Brazilian presalt carbonate reservoir located in the Santos Basin, who presents a complex and heterogenic geological setting with different sedimentological processes and diagenetic history. We generated metric flow units using the conventional core analysis and transposed to the well log data. Then, given a Markov chain Monte Carlo algorithm, the seismic data and the well log statistics, we simulated acoustic impedance, decametric flow units (DFU), metric flow units (MFU), porosity and permeability volumes in the metric scale. The aim is to estimate a minimum amount of MFU able to calculate realistic scenarios porosity and permeability scenarios, without losing the seismic lateral control. In other words, every porosity and permeability volume simulated produces a synthetic seismic that match the real seismic of the area, even in the metric scale. The achieved 3D results represent a high-resolution fluid flow reservoir modelling considering the lateral control of the seismic during the process and can be directly incorporated in the dynamic characterization workflow.

1. Introduction

Complex geology reservoir systems present many challenges to generate coherent static and dynamic models for reservoir simulation. The representation of reservoir heterogeneities and flow patterns comprehend the most important step to predict subsurface fluid movement, production and injection, especially in giant oil fields where prediction errors can result in a great loss of investment.

Flow units (FUs) reservoir rock typing can present an advantage over lithological rock typing in the 3D model building process using seismic data as a constraint, as FU provides better estimations of reservoir petrophysical properties, like porosity (ϕ) and absolute permeability (k), even in complex geological settings (Penna and Lupinacci, 2021). Once FUs may not have any relation with the lithology, incorporating FUs into reservoir models, which are essentially built with geological premises, is quite challenge for any asset team. Lithological facies, for instance, can comprehend two distinct FUs, depending on the diagenetic evolution of both rocks. Due to pore obliteration or generation processes, lithological facies would present different fluid flow and petrophysical patterns, and different consequences when submitted to production or injection (Penna and Lupinacci, 2020).

FU rock typing has been performed from flow zone indicator (FZI) (Nabawy et al., 2018), electrical parameters (Ghanbarian et al., 2018), FZI-star (Mirzaei-Paiaman et al., 2018; Rocha et al., 2019) and mercury injection capillary pressure (Liu et al., 2019), demonstrating how FUs are a powerful tool to predict storage and flow capacity of the reservoir, regardless of the geological complexity. Penna and Lupinacci (2021) showed that the 3D porosity and permeability performed on the basis of FU is a valuable and accurate tool to be incorporated into workflows in the construction of

* Corresponding author.
E-mail address: rpenna@petrobras.com.br (R. Penna).

https://doi.org/10.1016/j.petsci.2024.02.013

reservoir models.

Because of the FU incorporation difficulties and lack of correlation with lithological facies, most 3D static models built from FU are merely a geostatistical procedure away from the well control, without any lateral constraint of the facies interpolation (Li et al., 2017; Zhang et al., 2018). However, recent studies have incorporated seismic data into the FU modelling workflow for the FU interpolation. Iravani et al. (2018) considered the acoustic impedance as constraint for interpolation of petrophysical properties in a FU template. Yarmohammadi et al. (2014), Rastegarnia et al. (2016) and Hatampour et al. (2018) applied artificial intelligence to obtain linear relationships between FU and seismic attributes, creating their constraints to the FU facies modelling. Penna and Lupinacci (2021) used a cumulative S-curve analysis to create a decametric FU rock typing, and, through a Bayesian probabilistic model, performed 3D porosity and permeability, adequate to the seismic acoustic impedance resolution. All these seismic-generated FU models can later be successfully incorporated in the static modelling workflow of the reservoir, as hard constraints or secondary variable in co-kriging techniques.

The usage of seismic attributes provides lateral control for FU interpolation away from the well and is especially relevant in large reservoirs with a reduced number of drilled wells. However, the vertical resolution of deterministic seismic inversion products is limited to the decametric scale, above 20 m for Brazilian presalt reservoirs (more details in Penna and Lupinacci, 2021). In seismic-incorporated FUs and fluids movements detection, the scale of observation is crucial as, for instance, porous fractured media will be more or less connected depending on the grid size (Haridy et al., 2020). Conventional methods of seismic facies classification do not extrapolate the vertical resolution further from the input data limit. Considering that most of the FU classifications are made in the core scale (millimetric) and transposed to well log scale (centimetric), then several upscale and downscale assumptions are needed to incorporate the decametric seismic results (Penna and Lupinacci, 2021).

This paper proposes an approach to estimate seismic derived petrophysical property volumes at the metric scale. Using data percentiles and a cumulative S-curve from the core porosity and absolute permeability, we calculated a significant number of decametric and metric flow units that correlates with seismic acoustic impedance and responds for both large and small scales flow characteristics of the reservoir. Within each iteration of decametric and metric flow units from the geostatistical seismic inversion, we co-simulated petrophysical properties volumes that respect the well information in the metric scale and are laterally consistent with the local geology, regardless of the input resolution limit.

2. Study area and geological settings

Mero reservoir, part of the Libra block, is located in the northeast portion of the Santos Basil, Brazil (Fig. 1). The consortium that operates the field consists of Petrobras, Shell, Total, CNOOC and CNPC, under the new Brazilian production-sharing contract ruled by Pré-Sal Petróleo S.A. (PPSA). The initial exploratory phase of the block estimates an oil in place volume between 8 and 12 billion BOE (Carlotto et al., 2017), with high-complexity geology, igneous rocks occurrence (Penna et al., 2019; Penna and Lupinacci, 2020, 2021; Oliveira et al., 2021) and diagenetic effects (Leite et al., 2020; Sartorato et al., 2020). One of the main hydrocarbon fluid characteristics from Mero Field is the high CO_2 content (44% in the gas phase), which imposes several challenges to the reservoir management. The production design comprises a floating production storage and offloading (FPSO) designed to reinject all the gas produced (Moczydlower et al., 2019). The drilled wells by the consortium are keepers and will be used as producers or water alternating gas (WAG) injectors.

Santos Basin evolution history (also Libra block, consequently) initiates with basalts from Camburiú Formation (138–130 million years) as the response for the initial Gondwana breakup. Piçarras Formation (Barremian age) corresponds to the initial rift stage of the continental breakup, with sandstones, mudstones and shales deposited in lacustrine environments (Carlotto et al., 2017). From the Neobarremian until Eoaptian ages, rudstones from Itapema Formation were deposited in high energy platform settings. In lower energy settings, usually in relative structural low, organic rich shales occur. These rocks are considered the main hydrocarbon source in the Santos Basin (Moreira et al., 2007). The Barra Velha Formation deposits are from transitional environments between continental to shallow marine settings, the lower part to the intra-Alagoas unconformity still belongs to the rift phase and the upper part belongs to the sag phase (Buckley et al., 2015; Wright and Barnett, 2015; Neves et al., 2019). The base of the sequence are predominantly grainstones and packstones (reword facies), while in the top shrubs, spherulites and laminites (in-situ facies) occur more frequently (Gomes et al., 2020). In the late Aptian, already in marine environment, a thick salt sequence from Ariri Formation were deposited. This layer is the main Santos basin hydrocarbon seal and is mainly composed by halite and anhydrite (Moreira et al., 2007). Fig. 2 shows the Santos Basin presalt lithostratigraphy, tectonic evolution and unconformities adopted in this work.

Main reservoir rocks of Mero field are bivalve rudstones (coquinas) from the Itapema Formation and shrubs and spherulites from the Barra Velha Formation, although high porosity is also found in rework facies as bioclastic floatstone, grainstones and, packstones (Jesus et al., 2017; Penna and Lupinacci, 2020; Penna and Lupinacci, 2021). Several diagenetic effects of dissolution and neomorphism, replacement of minerals, silicification and dolomitization are identified, and correspond to the main effects that controls porosity generation and/or obliteration and, consequently, fluid movements in the reservoir (Herlinger et al., 2017; Gomes et al., 2020; Leite et al., 2020; Sartorato et al., 2020).

A unique feature of the Libra block and Mero reservoir is the abundant igneous rocks presence (Penna et al., 2019; Oliveira et al., 2021). Extrusive igneous rocks are of Barremian/Aptian age and mainly composed by tholeiitic basalts, more commonly found below Itapema Formation (Penna et al., 2019). Intrusive igneous rocks are of Santonian/Campanian ages, mainly alkaline, and can occur anywhere in the stratigraphy cutting surrounding rocks or concordant to the sedimentary layering (e.g., top of the Barra Velha Formation). The correct mapping and prediction of these rocks are very relevant for the characterization and management of the reservoir, once they penalize the total oil in place volume, they can act as flow barriers (or even high permeability layers, if fracturing is high enough) and contribute to the regional aquifer and pressure maintenance.

3. Data available

The consortium that operates the field performed an extensive core program with approximately 500 m of linear samples taken in both Barra Velha and Itapema formations. 1700 conventional core and plug analysis measurements of porosity and permeability are available in different stratigraphic levels from seventeen drilled wells. We organized and analyzed this datasheet for the purpose of flow unit classification. Twelve well logs are also available and comprehends sets of both logging while drilling (LWD) and wireline: gamma ray, resistivity, compressional and shear slowness, density, nuclear magnetic resonance porosities (total, effective and

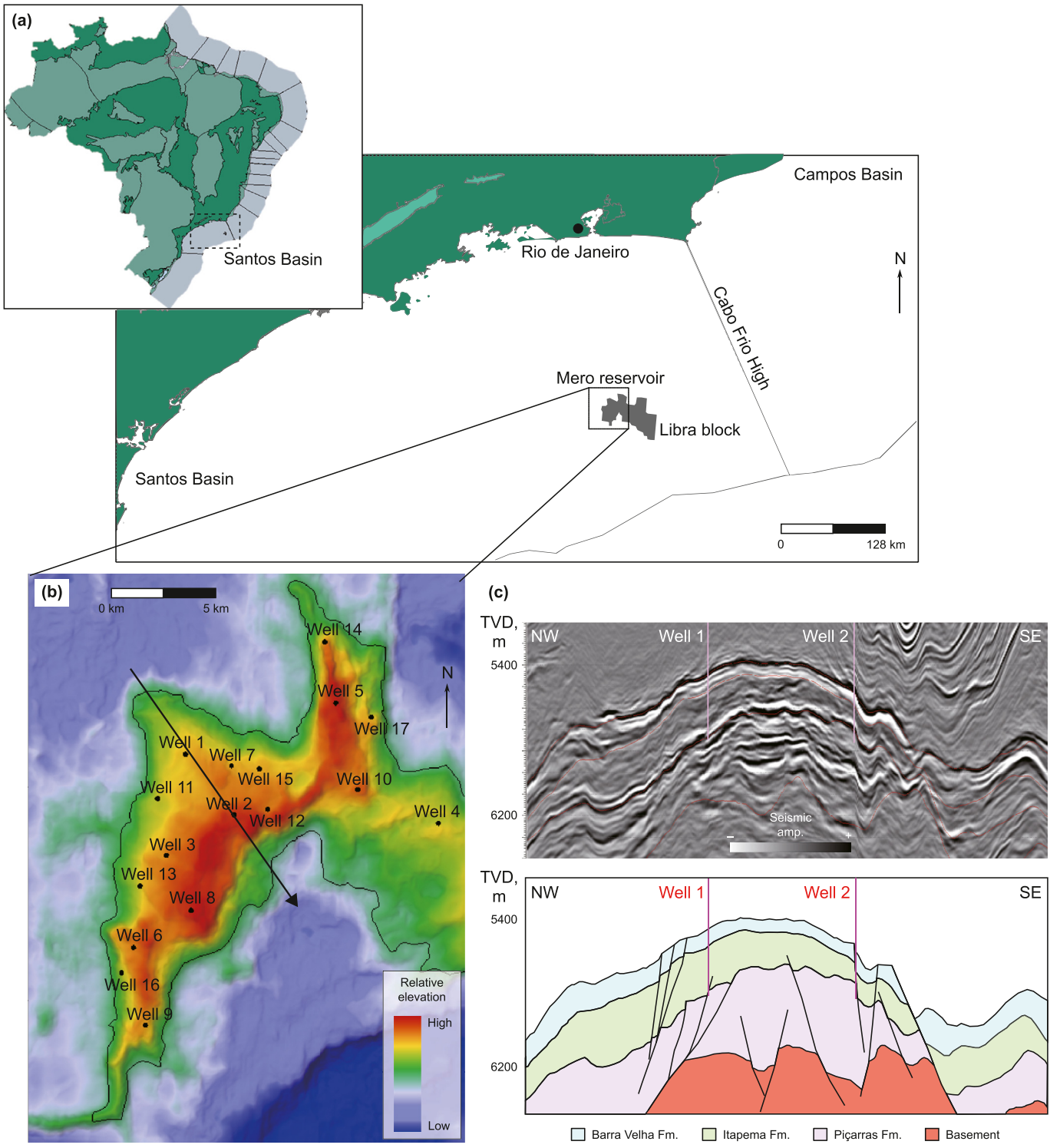

Fig. 1. **(a)** Mero reservoir and Libra block location in southeast Brazil. **(b)** Top of reservoir (Barra Velha Formation) structural map. **(c)** NW-SE seismic section a stratigraphic interpretation (after Penna and Lupinacci, 2021).

free fluid) and permeability and elements (e.g., calcium, potassium and magnesium).

The available seismic data is a legacy seismic acquisition that cover the whole Libra block with an 8 km streamer cable length, 6.25 × 25 m grid and 5 m of vertical sampling. This data was pre-stack reprocessed in 2016 with an initial tilted transversely isotropic (TTI) velocity model and a vertical transversely isotropic full waveform inversion (VTI-FWI) from 3 to 45 Hz. Then, a multi-layer tomography using both Kirchhoff and reverse time migration (RTM) picks was performed, followed by a TTI-FWI from 7 to 8 Hz applied at the entire geologic sequence (pos-salt, salt and presalt) as detailed by Araujo and Gouveia (2015). For the FWI velocity model, high and low-salt velocity layers, like anhydrite, tachyhydrite, carnallite and sylvinite, as well as igneous rocks,

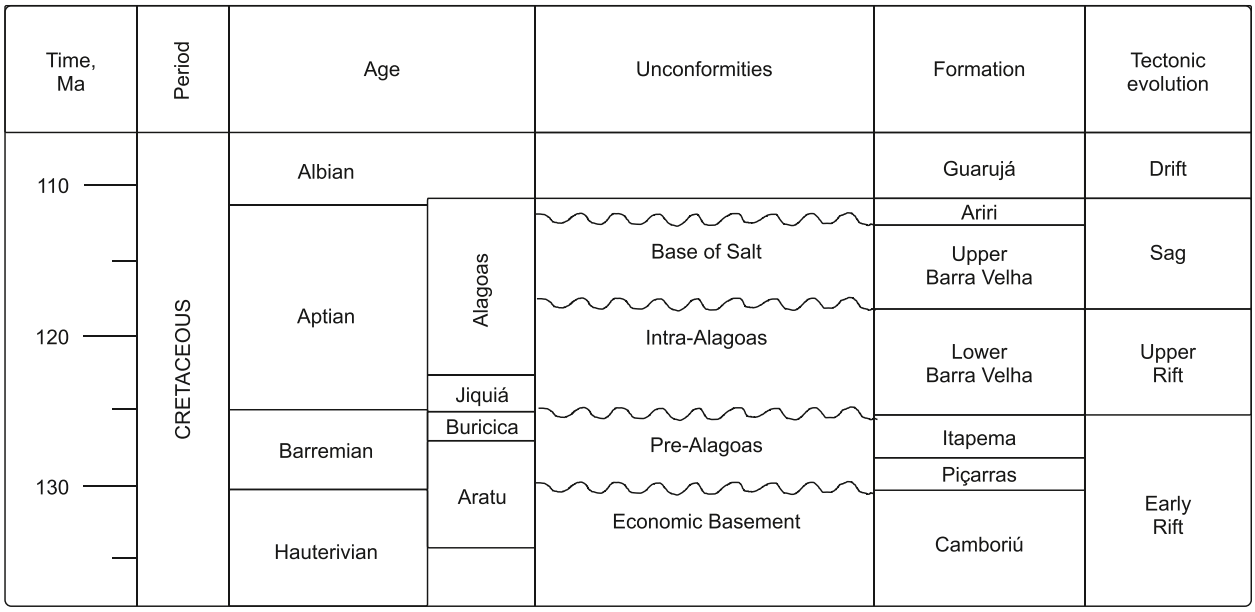

Fig. 2. Santos Basin presalt lithostratigraphy, tectonic evolution and unconformities (After Buckley et al., 2015; Wright and Barnett, 2015; Neves et al., 2019).

within the salt stratification, were incorporated. This procedure is presented and discussed and by Seifert et al. (2017).

In the presalt interval, the seismic data has approximately 15 Hz of peak frequency with bandwidth of 5–35 Hz. Based on the local geology petrophysical characteristics and the seismic spectral distribution, Penna and Lupinacci (2021) created a wedge model to estimate the vertical resolution of the full-stack seismic considering the true thickness resolving capacity. According to their analyses, the vertical resolution is 62 m when considering the seismic amplitude and 23 m from inverted acoustic impedance volume. Thus, any layer below these limits will be falsely estimated in terms of thickness. This means that facies or flow unit mapped from seismic amplitude or inverted acoustic impedance volumes will present decametric proportions.

4. Metric flow units facies discretization and rock typing statistics

Considering the amount of conventional core analysis available in the Mero reservoir, we used two methods based on permeability (k) versus porosity (ϕ) for flow unit discretization. First, we considered Gunter et al. (1997) stratigraphic modified Lorenz plot (SMLP) as a visual aid to estimate a minimum number of flow units and identify local reservoir flow trends in both decametric and metric scales. Then, we calculated rock quality index/flow zone indicator (RQI/FZI) for the discretization (Amaefule et al., 1993). Those are both extensively documented methods successfully applied in both clastic and carbonate geological settings.

The SMLP was first introduced by Gunter et al. (1997) by plotting the percent storage capacity (product of porosity and thickness) versus percent flow capacity (product of permeability and thickness), providing a visual guide to estimate how many FUs are necessary to honor the geologic framework in terms of fluid movement in the subsurface. Fig. 3 shows the SMLP plot of both Barra Velha and Itapema formations, using percentiles of all the samples for a cleaner display of the chart. The minimum number of the FU estimate is performed by observing the slope and behavior of the curve: as the mean storage and flow capacity increases, we have better flow units in terms of its permoporous characteristics.

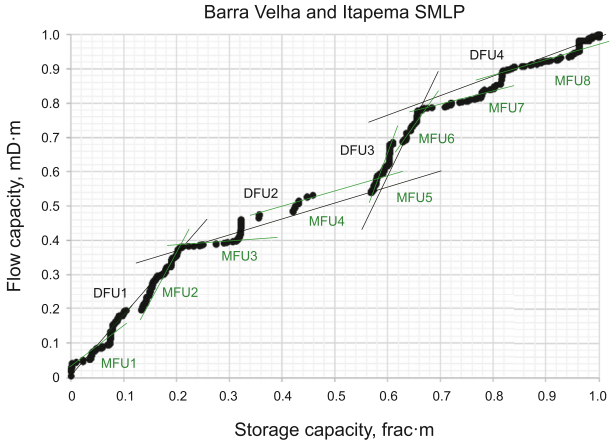

Fig. 3. Barra Velha and Itapema formations SMLP. Black lines represent decametric scale flow units, and green lines represent metric scale flow units. In this chart, storage capacity is the product of core porosity versus layer thickness, and flow capacity is the product of core permeability versus layer thickness. We considered this only as a qualitative plot, and a great visual tool for evidencing the scale-dependence of the petrophysical properties.

In that sense, flat segments can correspond to seals, baffle zones or low-production zones, as they may present some level of porosity, but have limited contribution of permeability. Steep segments correspond to "speed zones" of the reservoir, and they can have low or high porosity, but provide major contributions to the reservoir flow performance.

We estimated the minimum number of flow units in the SMLP using a sequence stratigraphy reasoning for high order and low order variations, like a Wheeler Diagram interpretation (Wheeler, 1958). The plot in Fig. 3 clearly demonstrates how the flow unit characterization is scale dependent. Variations of the low- and high-frequency cycles are correlational since the slope of the low frequency curve depends on the constructive effect of each high frequency curve. Penna and Lupinacci (2021) introduced a workflow for the detection of decametric flow units using inverted acoustic and shear impedance volumes, considering the black lines

as decametric trend (Fig. 3). However, our purpose here is to characterize higher orders of fluid movements in the reservoir as metric flow units using the acoustic impedance as constraints obtained from a geostatistical seismic inversion. For this, eight FU are considered as metric flow trends (green lines) in Fig. 3. SMLP are used, in this work, only as a visual guide for this scale-dependence of the petrophysical properties.

The flow unit discretization is performed in the core analysis using the rock quality index/flow zone indicator (RQI/FZI), and then transposed to the well log data. This method is based on permeability in mD and effective porosity (ϕ_E) ratio and derived from a generalization of the Kozeny-Carmen equations (Kozeny, 1927). It was introduced by Amaefule et al. (1993) and is widely used due to its simplicity and assertive results. Let the index RQI (reservoir quality index, in μm) be

$$\mathrm{RQI} = 0.0314 \cdot \sqrt{\frac{k}{\phi_E}}, \tag{1}$$

where k is the absolute permeability (in mD) and ϕ_E the effective porosity. Then, the FZI is given by

$$\mathrm{FZI} = \frac{\mathrm{RQI}}{\phi_Z}, \tag{2}$$

where ϕ_Z is an effective porosity normalization on the form $\phi_Z = \phi_E / 1-\phi_E$. Since its derivation from Kozeny-Carmen equations, FZI value is approximates an average pore throat radius for a given porous media, relating effective porosity and permeability. Different sedimentation environments, late diagenetic processes and reservoir geometry are also controlling parameters of FZI (Tiab and Donaldson, 2004).

Taking log on both sides of Eq. (2) and rearranging it, we verify the linearity between FZI, RQI and ϕ_Z:

$$\log\mathrm{RQI} = \log\mathrm{FZI} + \log \phi_Z. \tag{3}$$

In log-log plot of the RQI versus ϕ_Z, a constant value of the FZI produces an inclined straight line. The inference is that samples with similar flow behavior falls around a corresponding slope line, determining a single flow unit (FU). Samples with distinct flow characteristics are plotted in different parallel lines and arrange distinct flow units.

Different methodologies for clustering samples around FZI values and creating FU are available in the literature and applied in different geological scenarios. In some cases, a simple log (FZI) histogram discretization is enough to discretize the flow units (considering that the samples show strong FZI versus permeability correlation and a log-normal FZI distribution). More complex methods, such as iterative multi-linear regressions (Al-Ajmi and Holditch, 2000) and normal probability plots (cumulative distribution function, Mahjour et al., 2016) are also widely used, especially in more complex geological settings. Penna and Lupinacci (2020, 2021) showed that the usage of percentiles and a cumulative S-curve produced a significant minimum amount of flow units with statistical relevance, without compromising the estimation of petrophysical properties. This is particularly relevant to the scope of this study, considering the amount of k and ϕ measurements, the high complexity degree of the Mero reservoir, and the aim to correlate the FU to seismic data with respect to its vertical resolution limit.

The steps to construct the RQI/FZI cumulative S-curve, as presented by Penna and Lupinacci (2021), are.

1. Take all the core porosity and permeability measurements and calculate statistical relevant percentiles (the number varies depending on the data characteristics). Each percentile is a representative sample from a given interval.
2. Calculate RQI and FZI values using Eqs. (1) and (2) and the percentiles values.
3. Order the data with increasing values of log (FZI).
4. Accumulate and normalize the percentiles of permeability values.
5. Calculate the slope of the curve for each sample (Fig. 4).

As described in the SMLP, at least two scales of variations are observable in the derivative data (Fig. 3): one on a small scale (higher order), related to metric variations, and other on a large scale (lower order), related to decametre variations. Penna and Lupinacci (2021) chosen to interpretate the major jumps in the slope curve as the decametric flow characteristics changes in the reservoir, although this can be extended to many scales. The lower scale of observation responds to low frequency variations in the SMLP and FZI S-curve plots, and higher order of variations responds to high frequency variations. This was fit for purpose, as the scope of their work were to characterize flow units in the decametric scale and then correlate with elastic attributes. Given that the aim

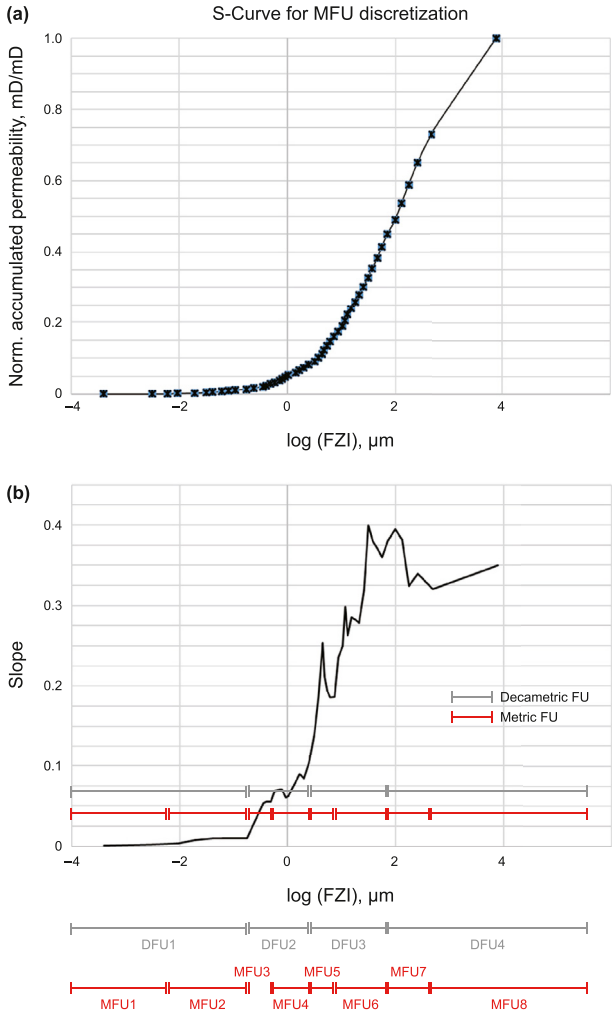

Fig. 4. The log (FZI) S-curve for MFU discretization. Grey line corresponds to decametric FU classification (after Penna and Lupinacci, 2021) and red line corresponds to metric FU classification.

of the present study is to get a step further, discretizing metric flow units with the seismic data, we interpret the major jumps in the slope plot, first order variation, that corresponds to the decametric FU, same as Penna and Lupinacci (2021), and the second order variation, as the metric FU.

Using both effective porosity and permeability from the nuclear magnetic resonance (NMR) well logs, the RQI/FZI values are calculated for each well through Eqs. (1) and (2). The discretization of the FU in the metric (MFU) and decametric (DFU) scales from the FZI S-curve plot is shown in Fig. 4. Eight metric flow units are interpreted considering the changes in the FZI S-curve slope. Note that the number of metric flow units correlates to the SMLP interpretation as a higher order variation from the decametric scale. The cut-offs in log (FZI) used for discretizing the flow metric units (MFU) are shown in Table 1.

The initial flat segment parallel to the X axis of the FZI S-curve (Fig. 4) describes FUs that have no contributions to the flow behavior in the metric scale. Therefore, MFU1 and MFU2 are considered seals or baffle zones that retain fluid flow, acting as vertical and horizontal barriers. In general, rocks with reduced matrix porosity like igneous rocks, cemented and clayey carbonates are into these units.

MFU3 is denoted by the initial detachment of the curve from the X axis, and, subsequently, MFU4 (Fig. 4). These FUs have some flow capacity but are very poor in terms of overall reservoir flow behavior. This is the typical behavior of carbonates with some late diagenetic effects, like quartz and dolomite cementation obliterating the original matrix porosity of the rock. Although not directly considered for production, they are important for maintaining reservoir pressurization over production time.

MFU5 and MFU6 are the first ramp up of the curve (Fig. 4), with better permoporous reservoir characteristics then the previous units. Although some level of diagenetic effect can occur, they will have considerable contributions to reservoir flow during production. Some bioclastic grainstones, packstones and wackestones belongs to MFU5 and MFU6, for example. The end of the curve corresponds to the better FUs in terms of permoporous characteristics, MFU7 and MFU8. They have considerable porosity and remarkable flow performance during production. In general, MFU7 and MFU8 correspond to clean calcite carbonates like bivalve rudstones (coquinas) from the Itapema Formation and shrubs and rework facies from the Barra Velha Formation, with little or none late diagenetic effects (Penna and Lupinacci, 2021).

Fig. 5 demonstrates how the new classification differs from the decametric flow unit (DFU) considering the seismic vertical resolution limitation. The relationship between DFU1 and MFU1 and MFU2, for instance, are quite notable, as the latter are a one-step upscaling of the first one. The mean, median and standard deviation of the acoustic impedance (PI), effective porosity (ϕ) and Schlumberger-Doll Research (Al-Ajmi and Holditch, 2000) permeability (k) for each metric flow units are displayed in Table 2. These calculations were performed using the well logs. Note that the overall values of the PI tend to decrease from MFU1 to MFU8, while porosity and permeability increase. This is expected, as MFU1 corresponds to low-FZI values (small pore throat radius) and MFU8 has high-FZI values (large pore throat radius). In general, the distribution of PI, porosity and permeability for MFU are close to symmetric, with little mean versus median differences.

Table 1
Metric FU (MFU) cut-offs from the FZI S-curve.

	log (FZI) values
MFU1	below −2.2
MFU2	−2.2 to −0.5
MFU3	−0.5 to −0.2
MFU4	−0.2 to 0.4
MFU5	0.4 to 0.8
MFU6	0.8 to 1.9
MFU7	1.9 to 3.7
MFU8	Above 3.7

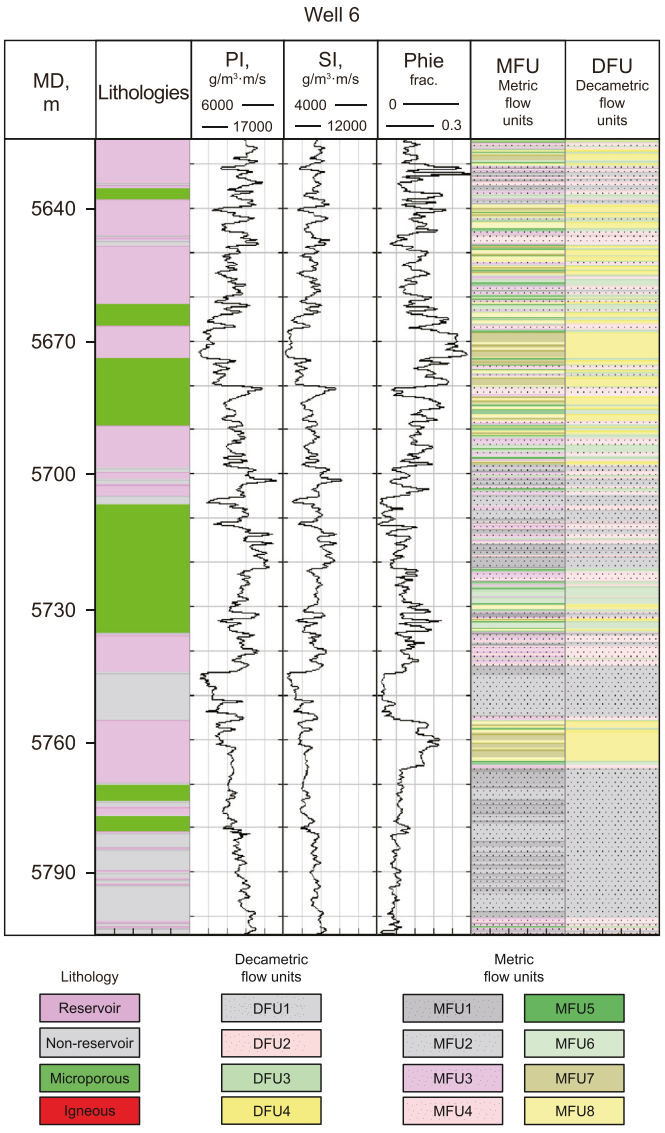

Fig. 5. Application of log (FZI) cut-off discretization in Well 6 using the effective porosity from the magnetic resonance data. Lithologies on the left correspond to a simplified classification for seismic facies analysis purposes (after Penna et al., 2019).

5. Geostatistical seismic inversion for metric flow units

5.1. Stochastic seismic inversion method

Geostatistics is a modelling tool that plays an important role in building earth models. In geoscience, initially developed with the constant grow of the mining industry, geostatistical concepts and algorithms have been widely adopted in the oil exploration and production for many purposes (Pereira et al., 2017; Feng et al., 2018; Ferreira and Lupinacci, 2018; Kneller et al., 2019; Peçanha et al., 2019). These techniques are traditionally used to interpolate the target property, most commonly facies, porosity and permeability,

Table 2
Mean, median and standard deviation (std. dev.) of the acoustic impedance (PI), porosity (ϕ) and permeability (k) from MFU1 to MFU8 considering both Barra Velha and Itapema formations.

		PI, g/cm^3·m/s	ϕ, frac.	k, mD
MFU1	mean	16,521	0.042	0.016
	median	17,478	0.044	0.005
	std. dev.	2785	0.019	0.022
MFU2	mean	14,829	0.087	0.265
	median	15,276	0.082	0.234
	std. dev.	1880	0.005	0.126
MFU3	mean	14,482	0.102	1.251
	median	14,869	0.102	1.057
	std. dev.	18,645	0.007	0.634
MFU4	mean	13,874	0.119	5.933
	median	14,112	0.118	5.658
	std. dev.	1850	0.004	2.023
MFU5	mean	13,047	0.144	28.23
	median	13,814	0.144	25.85
	std. dev.	1646	0.009	12.69
MFU6	mean	11,928	0.167	80.29
	median	11,022	0.168	78.01
	std. dev.	1599	0.004	16.77
MFU7	mean	11,522	0.188	232.75
	median	10,874	0.188	199.08
	std. dev.	1454	0.007	103.68
MFU8	mean	10,633	0.236	1760.67
	median	9830	0.220	1146.70
	std. dev.	1674	0.038	1425.33

between well data within a stratigraphic framework. The most common method is the sequential gaussian simulation (SGS, Deutsch and Journel, 1992).

Since the introduction by Haas and Dubrule (1994), stochastic seismic inversion is an active topic of interest, as the technique introduces seismic data as a constraint to generate possible earth models (Doyen, 2007). However, the direct use of seismic as secondary data for reservoir modelling is usually frustrating because of vertical scale differences between seismic (usually decametric resolution) and well logs (centimetric). Finding a relationship between, for instance, seismic amplitude and/or impedance volumes and well log porosity is constantly difficult, making the incorporation of seismic data directly into the SGS workflow a challenge for reservoir characterization (Azevedo and Soares, 2018).

The most documented and used methods for stochastic seismic inversion are SGS (Escobar et al., 2006), direct sequential simulation (DSS, Soares, 2001), global stochastic inversion (GSI, Soares et al., 2007) and Monte Carlo Markov Chain (MCMC Statmod® MC™, Sams et al., 2011). Although these methods differ in how to sample a prior/posterior pdf, they essentially produce multiple realizations of petrophysical properties, considering the stratigraphic grid and a given vertical sampling (that can be smaller than the available seismic sampling). Every iteration produces a geologic model that fits the seismic and well log data, i.e., each realization is plausible samples of the reservoir's posterior distribution and a variance measure of the input parameters, considering the seismic data as constrains.

In this study, we perform a Metropolis-Hastings (MH) algorithm within the MCMC method (MCMC Statmod® MC™, Sams et al., 2011) to simulate the acoustic impedance. There are three main steps in the stochastic inversion workflow, which are detailed further: 1) Statistical modelling, where are estimated the probability density functions (pdfs), variograms and trends for each decametric and metric facies; 2) Bayesian inference, combining the prior model, seismic and well data for compute the posterior distribution; 3) Sampling, where we used the MH-MCMC algorithm for sampling the posterior pdfs. Briefly, the algorithm builds a pdf that represents P(reservoir | geostatistics, seismic) and sample it for the target property volumes using the MCMC method, i.e., the probability of the produced reservoir model given the input geostatistics and seismic data.

The workflow for the stochastic seismic inversion is represented in Fig. 6. The evidence and assumptions are expressed as a series of pdfs defined over the property volumes. We calculated variograms for continuous and discrete properties and property distributions (multivariate joint pdfs). Then the seismic data is modelled for acoustic impedance using the convolutional model, and a normal pdf for the seismic noise is calculated directly in the seismic data (windowed in the reservoir area) to account for seismic noise, there is, uncorrelated differences between real and synthetic seismic (Saussus and Sams, 2012; Kneller et al., 2019). This parameter is directly correlated to the likelihood parameter of the inversion. The steps (Fig. 6) are described as.

I. In the stratigraphic grid, created from seismic horizons, start with an arbitrary reservoir model (res_0) and select a random location in the volume (the current state of the chain). The lateral sampling is consistent with the seismic data grid and the vertical sampling is 1 m.
II. Randomly generate a modified realization (res_1). A synthetic seismic ($synth_1$) is calculated through convolution between the estimated wavelet and res_1 acoustic properties. Considering the Bayesian inference scheme, compute the likelihood function of res_1 given the real seismic data: P(seis|$synth_1$).
III. Evaluate the prior distribution of the modified realization (P(res_1|geostats), which reflects the lateral and vertical continuity computed from the variograms and the value of the property at neighboring cells.
IV. Multiply the prior distribution P(res_1|geostats) with the likelihood function P(seis|$synth_1$) to compute the posterior probability value given the input information (e.g., statistics, well data, seismic horizons and stratigraphy). This step is the Bayesian inference of the algorithm.
V. Compare the posterior probability value with the current reservoir model res_0. If the proposal res_1 has a posterior probability value higher than res_0, there is, P(res_1|geostats, seis) > P(res_0|geostats, seis), then res_1 is accepted and the chain moves to a different random location considering res_1 as the new current state. Otherwise, if the value is smaller, res_1 can be randomically rejected (and res_0 is the current stat for the next step) or accepted as a ratio between P(res_1|geostats, seis) and P(res_0|geostats, seis). Note that this part is the Metropolis-Hastings of the algorithm, avoiding the calculation to be stuck in local maxima/minima as lower probabilities are sometimes accepted.
VI. The process continues updating for the entire seismic volume until P(res_n|geostats, seis) is no longer changing. Due to the large number of calculations needed to sweep the entire volume, the MCMC algorithm only calculate the conditional posterior pdf on a small portion of the volume at a time. Combination them all gives the global posterior pdf.

Note that the MCMC algorithm does not change the whole res_0 trace considering a single iteration. Instead, a small portion of the grid is modified a step at a time, until the entire grid is swept. All the pdfs are local, so they are re-calculated every time it moves to another part of the volume.

For our purpose, the stochastic seismic inversion fits very well, once we are taking advantage over the seismic constraint in

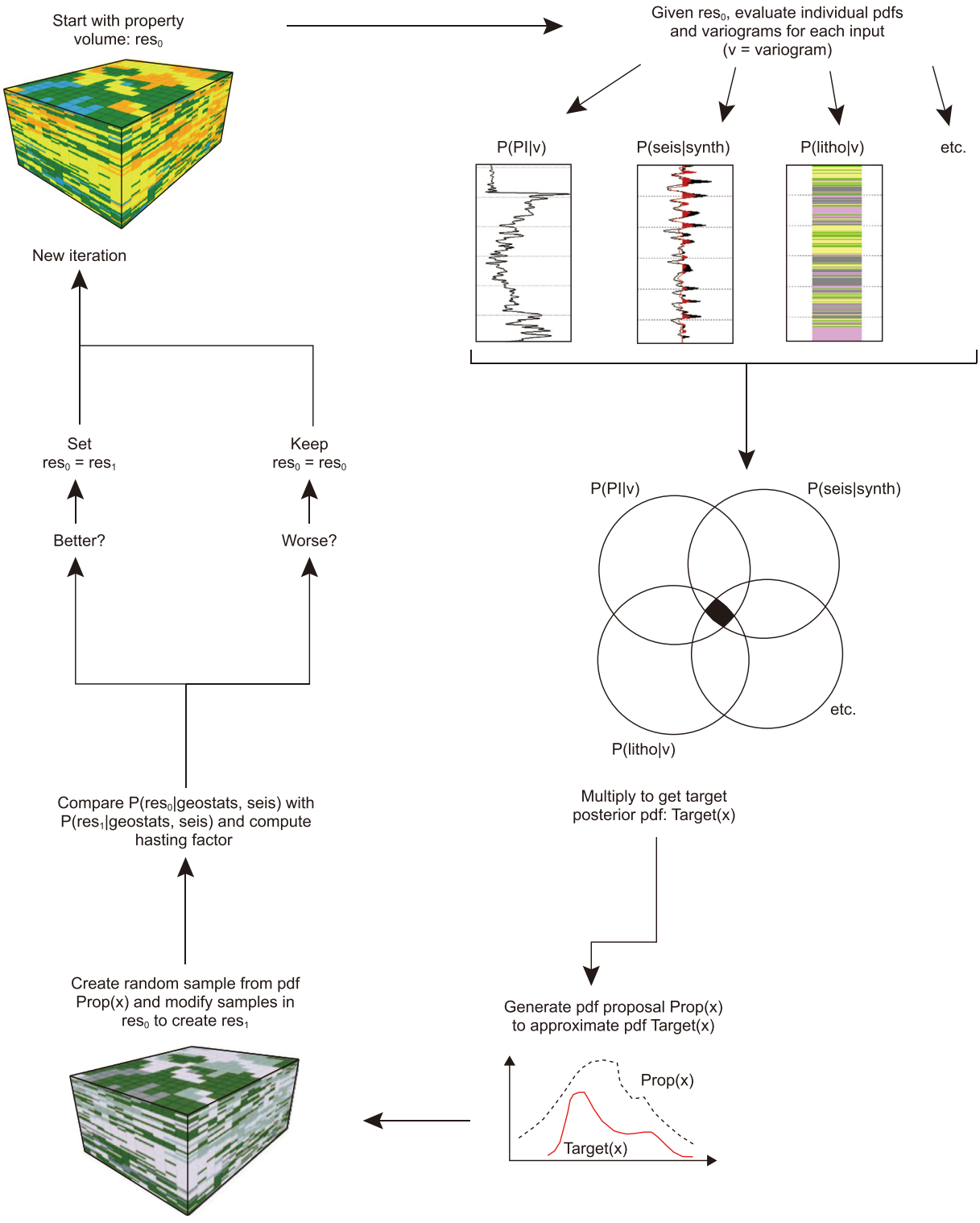

Fig. 6. MCMC Statmod® MC™ algorithm workflow.

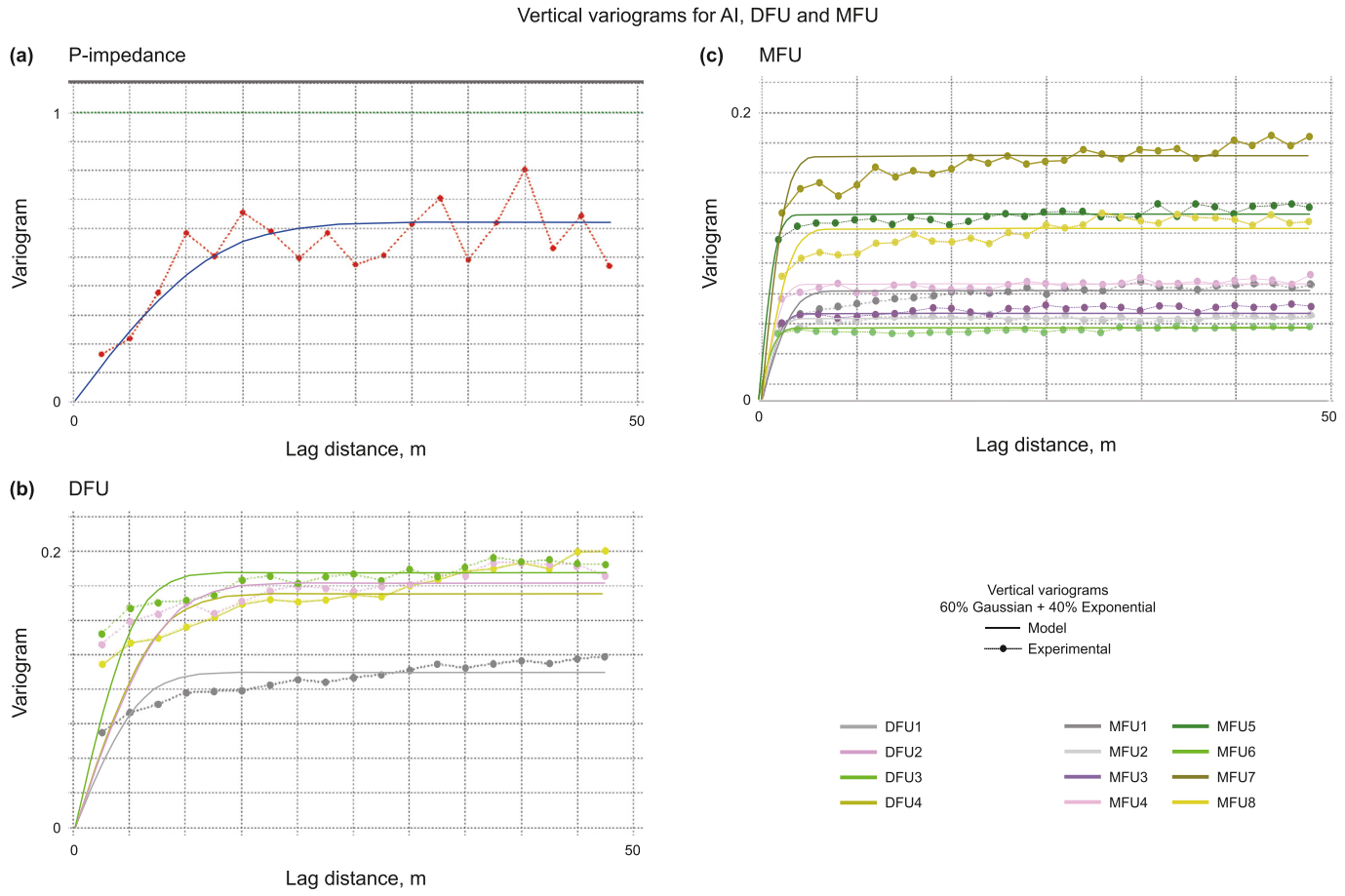

Fig. 7. Experimental and modelled vertical variograms for **(a)** acoustic impedance, **(b)** decametric flow units and **(c)** metric flow units. Experimental variograms were calculated from well logs.

decametric scale and explicitly simulating flow units in the metric scale, below the seismic data resolution. The objective is to generate many plausible flow units models (and consequently porosity and permeability models) in the decametric and metric scales, given the geostatistics associated with every metric flow unit (MFU).

5.2. Inputs and parametrization

We created the grid using three seismic horizons: the tops of the Barra Velha, Itapema and Piçarras formations (Fig. 2), where the first and last horizons represent respectively top and bottom of the reservoirs. The lateral spacing is relative to the seismic grid (25 m × 25 m), and vertical sampling is set to 1 m. The stochastic

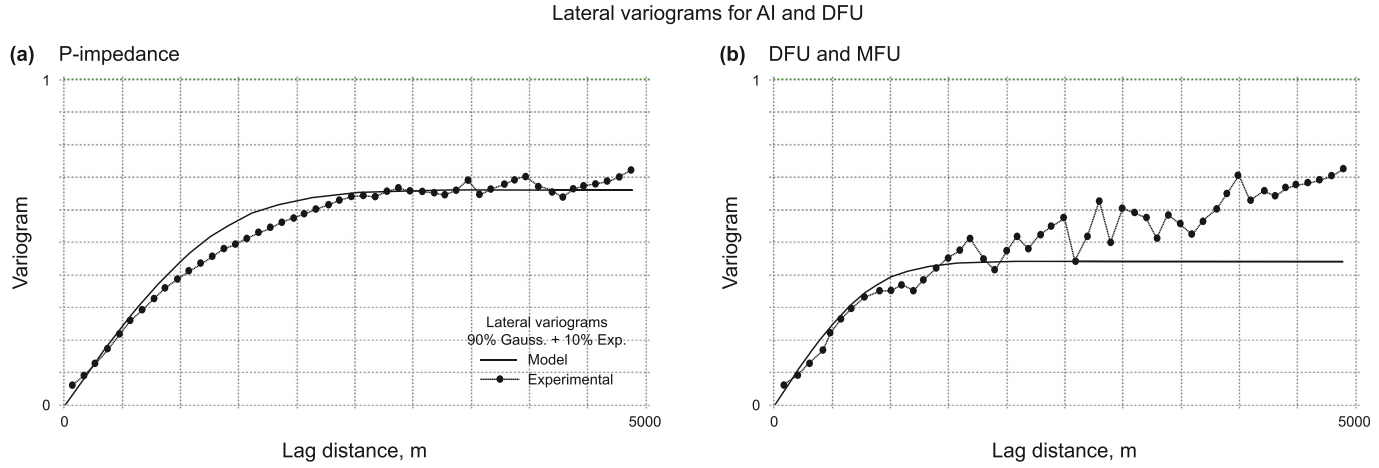

Fig. 8. Experimental and modelled lateral variograms for the **(a)** acoustic impedance and **(b)** decametric and metric flow units. We calculated the experimental variograms considering elastic inversion volumes (PI) (Penna et al., 2019) and Bayesian facies classification (DFU and MFU) (Penna and Lupinacci, 2021).

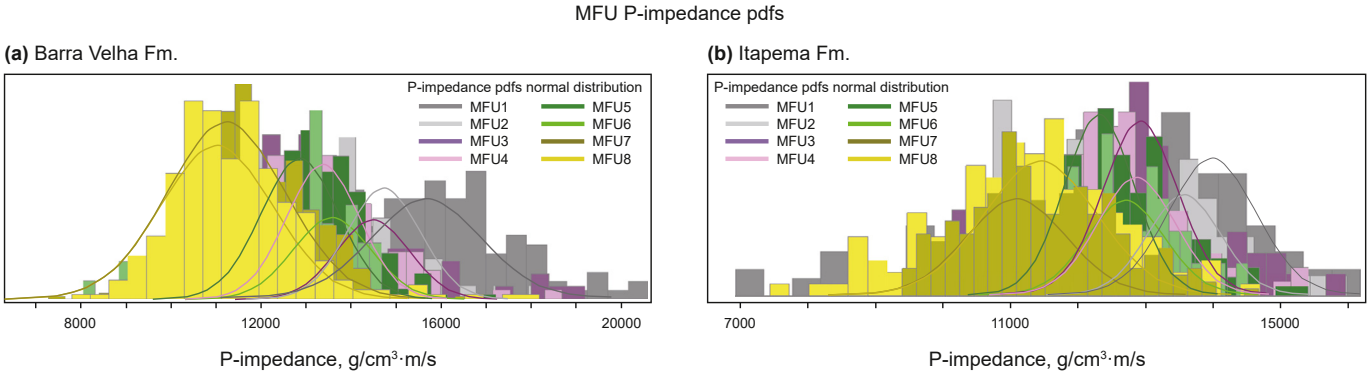

Fig. 9. P-Impedance pdfs for the MFU in the Barra Velha **(a)** and Itapema **(b)** formations.

seismic inversion is set to obtain the acoustic impedance and decametric and metric flow units (defined from the FZI cut-offs described in Table 1). We maintain the FZI S-curve relation between decametric and metric flow units, that is, MFU1 and MFU2 will only occur if DFU1 is present, for instance. This is compatible to the flow multi-scale of observation reasoning used for discretization.

We used experimental vertical variograms calculated from well logs for acoustic impedance, decametric and metric flow units. Fig. 7 shows an example of the experimental and modelled variograms. They are a mixture of 60% gaussian and 40% exponential with vertical range of 20 m for PI, of 5–10 m for DFU and of 3–6 m for MFU. No differences were observed between vertical variograms of the Barra Velha and Itapema formations, so we considered the same variogram parametrization for both layers.

Experimental lateral variograms were calculated through different maps. For the acoustic impedance were extracted the mean values for both Barra Velha and Itapema formations, considering the PI volume obtain from the elastic inversion (Penna et al., 2019). For the lateral variograms of the decametric flow units, we used the mode considering each of the most likely facies volumes derived from the Bayesian classification (Penna and Lupinacci, 2021). Both lateral variograms were calculated along the main Mero structural direction, NE-SW. The same DFU lateral variograms were considered for the MFU. Also, no considerable difference was found between lateral variograms of the Barra Velha and Itapema formations, therefore we used the same variograms for both formations. In general, they are a mixture between 90% Gaussian and 10% exponential curves with a range around 2500 m for the PI and 1000 m for DFU and MFU (Fig. 8).

Acoustic impedance pdfs for DFU are the same as shown in Penna and Lupinacci (2021). For MFU, we estimated normal PI pdfs for the Barra Velha and Itapema formations, as shown in Fig. 9. Due to the high resolution of the discretization, it is expected that the PI

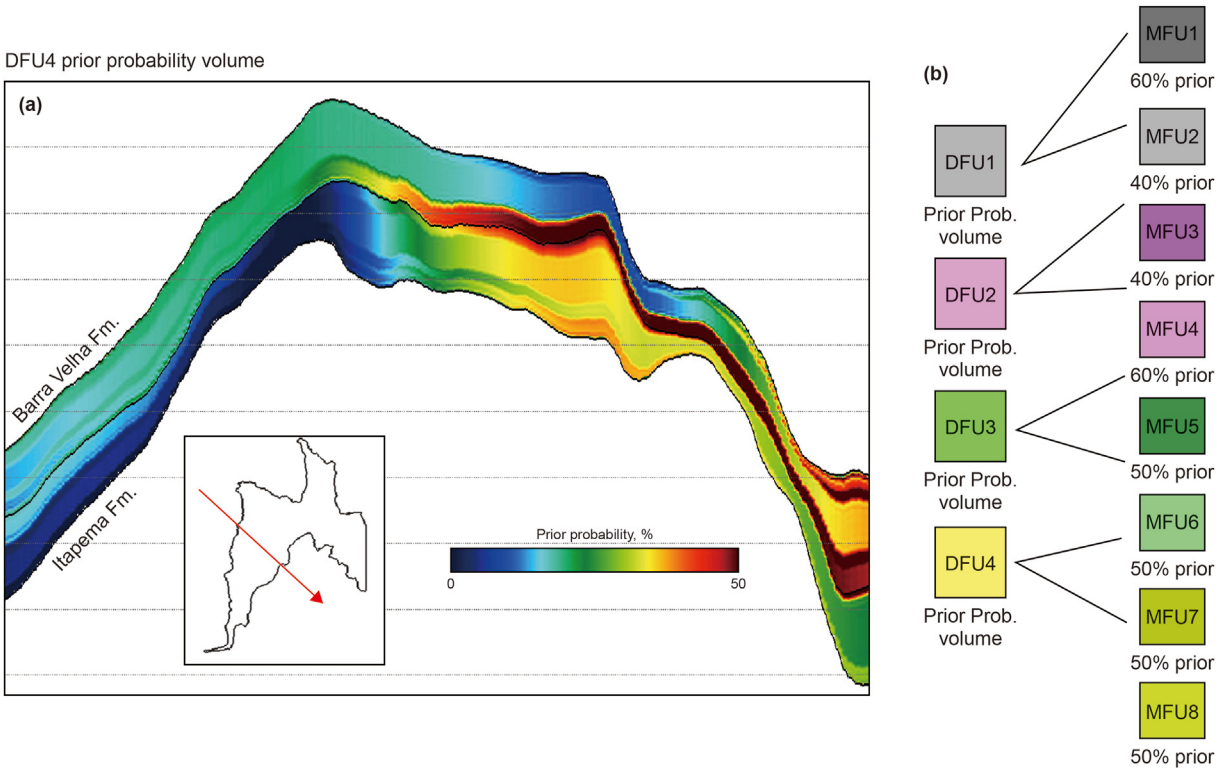

Fig. 10. **(a)** Prior probability NW-SE section through DFU4 3D volume and **(b)** the relation between prior probabilities of the DFU and MFU.

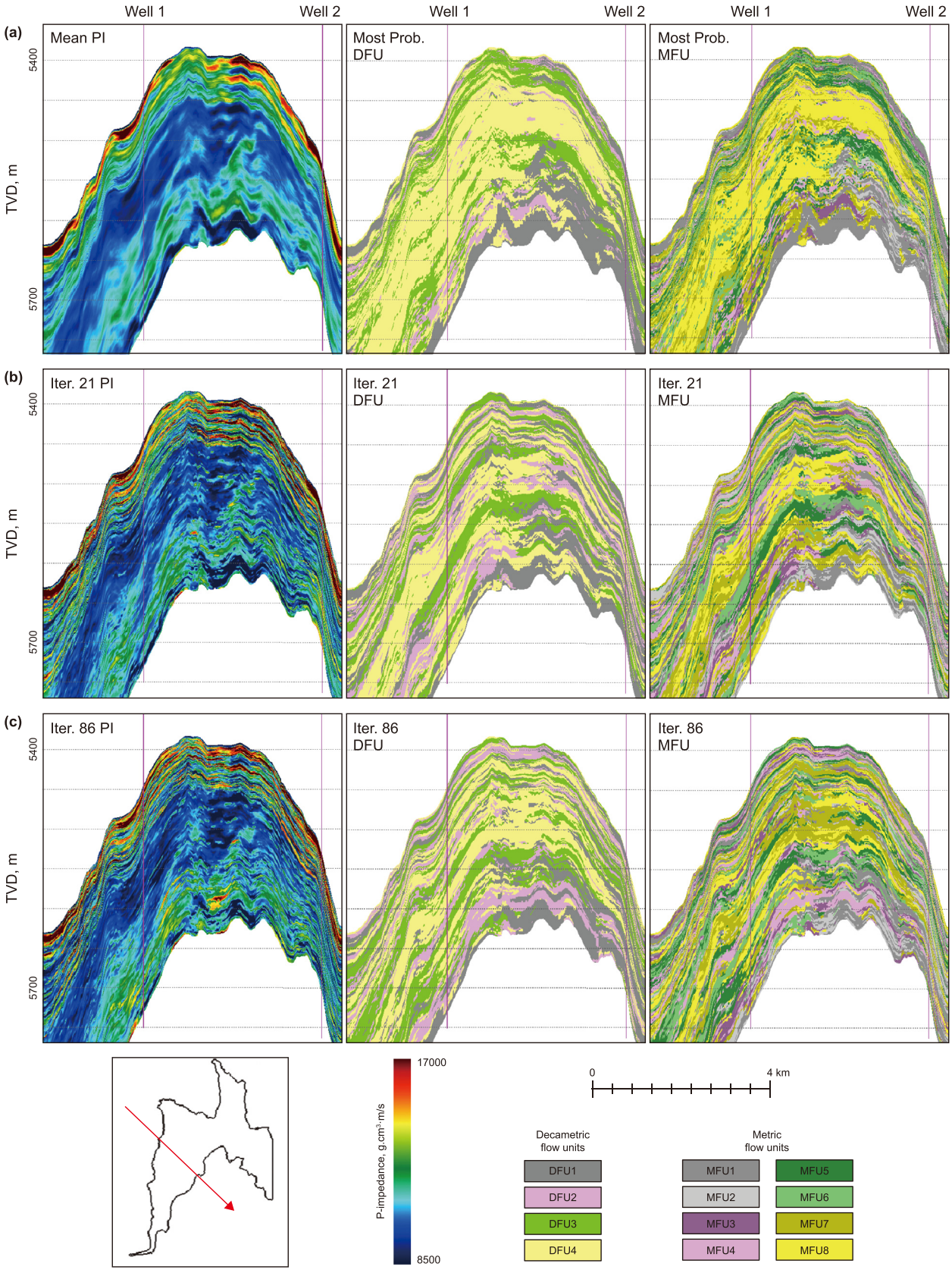

Fig. 11. **(a)** Mean PI and most probable DFU and MFU NW-SE section from 100 MCMC iterations. Iterations 21 **(b)** and 86 **(c)** PI, DFU and MFU results.

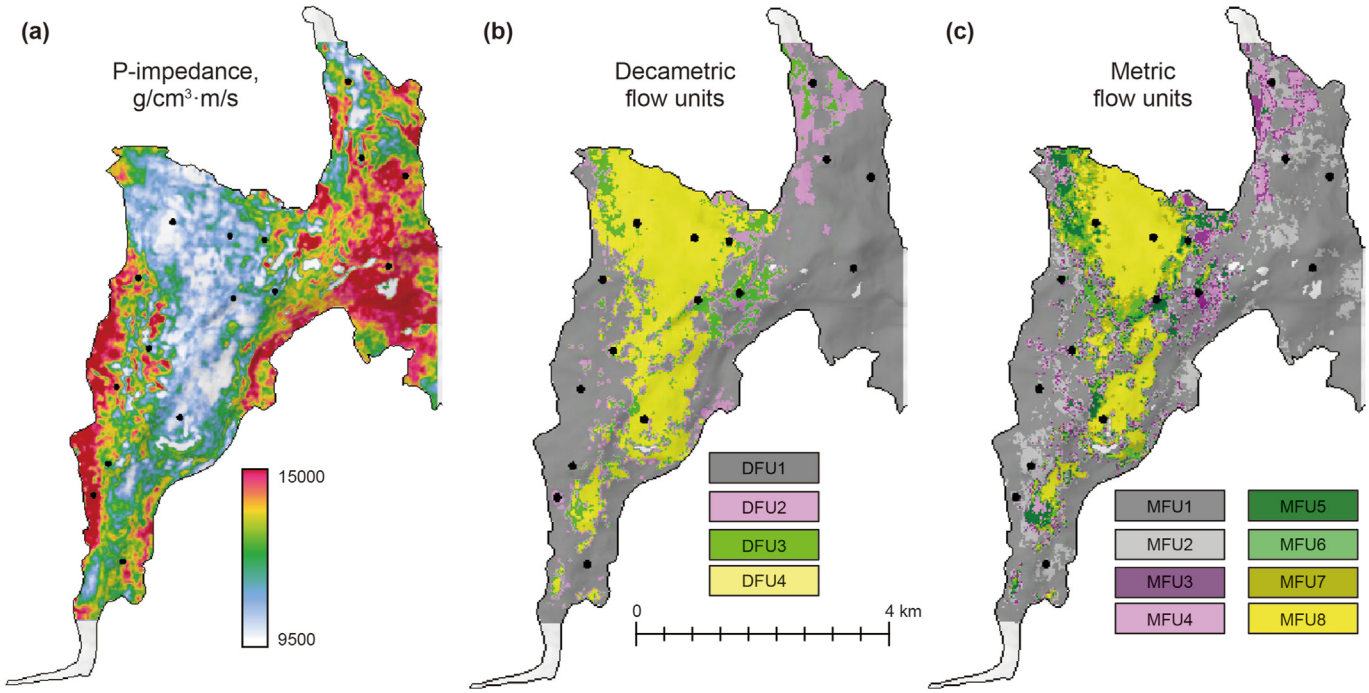

Fig. 12. (**a**) Mean PI map from the upper Itapema Formation. (**b**) DFU and (**c**) MFU mode maps from the same stratigraphic layer.

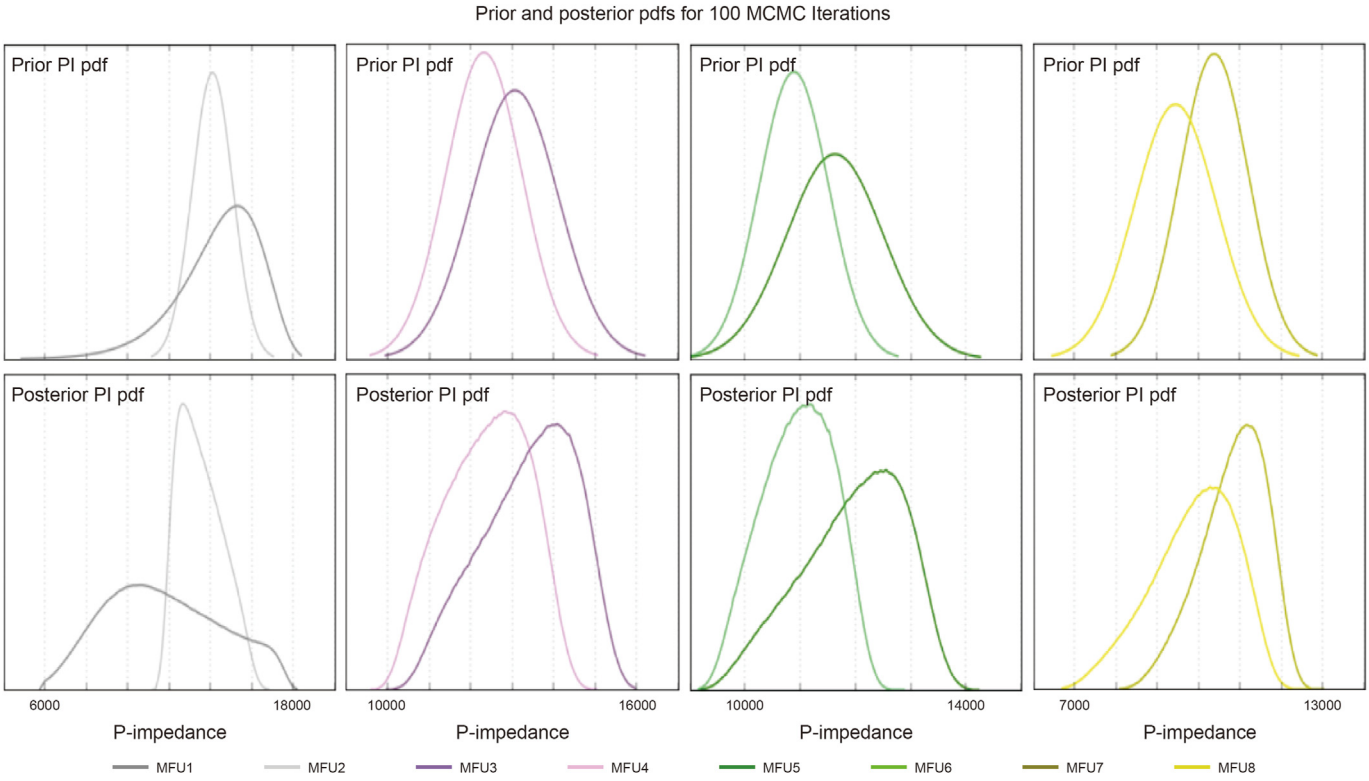

Fig. 13. Prior and posterior pdfs for the 100 MCMC iterations. MFU1 posterior pdfs deviates from prior pdfs because of the increasing MFU1 occurrence in structural depressions, areas without any drilled wells sampling mud sediments, usually worse permoporous units with low PI values.

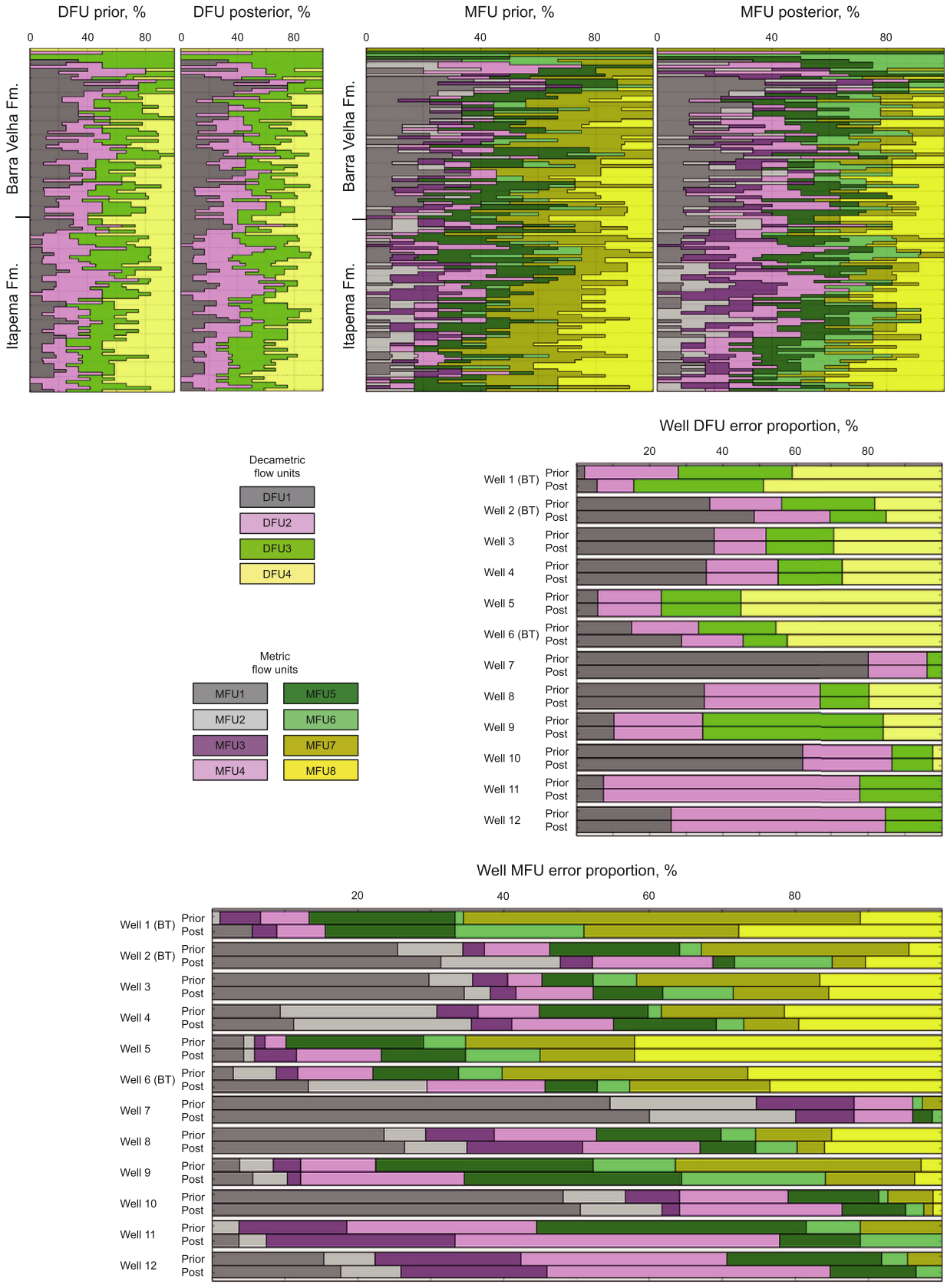

Fig. 14. Mean prior and posterior proportions for DFU and MFU considering 100 MCMC iterations. Wells marked with BT were considered as blind tests for the inversion.

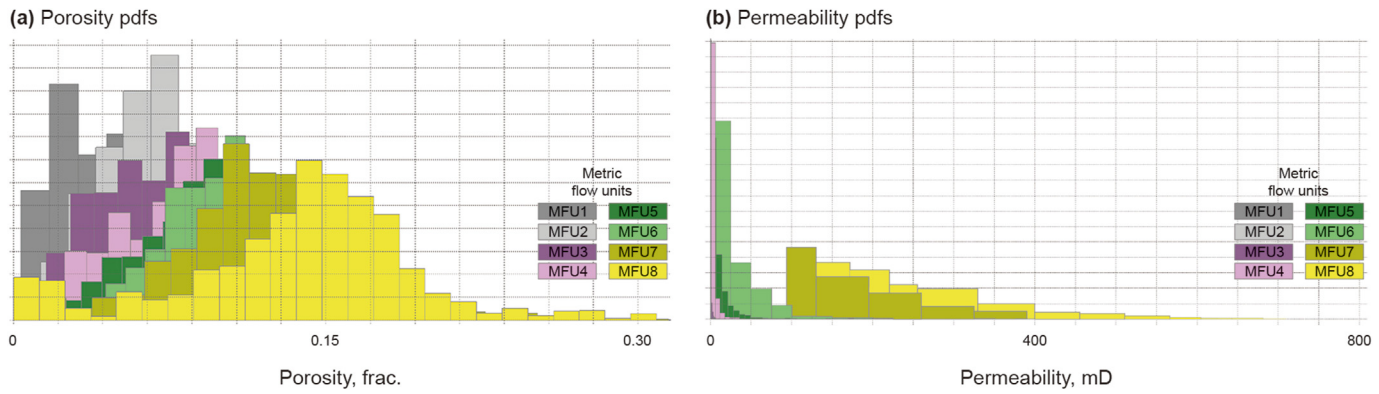

Fig. 15. Porosity **(a)** and permeability **(b)** pdfs for the cosimulation. MFU1 and MFU2 are concentered along the zero-permeability axis. Both Barra Velha and Itapema formations show the same behavior.

superimposition between MFU units is larger than the DFU pattern. One of the aims is solve this ambiguity through MCMC simulations and several iterations, producing a numerous amount of possible MFU occurrence volumes constrained to the seismic data in decametric scale. The general behavior observed concentrates more MFU1 in higher PI values and MFU8 in lower PI values, like the DFU behavior.

We chose not to use a constant value for the priori probability in the Bayesian classification, as the facies are highly heterogenous in carbonate environments. Instead, we constructed volumes regarding the laterally variable priori probability for each DFU extrapolating, through ordinary kriging, the facies. In the wells considering horizons and framework. Since there are no wells drilled in structural lows (therefore sampling low-energy settings) in the study area, we applied a multiplier to raise the prior occurrence probabilities of worse permoporous DFU and MFU away from the Mero main structural high. This behavior is corroborated by numerous presalt analogs that drilled this specific setting (Lima and De Ros, 2019; Neves et al., 2019; Gomes et al., 2020). For each DFU occurrence, there is a prior probability of MFU that corresponds to a mean ratio between its correlated facies obtain from the well data. For example, if DFU1 occurs in a given location, a prior probability for MFU1 is 60% and 40% for MFU2. Fig. 10 exemplifies how a prior probability varies laterally for DFU4, for exemplification, and a prior probability ratio from MFU1 to MFU8 considering the occurrence of each associated DFU.

5.3. Stochastic seismic inversion results and quality control (QC)

We performed 100 iterations for the MCMC stochastic seismic inversion, that is, 100 possible solutions were calculated for the acoustic impedance, DFU and MFU given the seismic data as constraint. The mean wavelet, necessary for the synthetic seismic convolution, is the same used for the seismic inversion by Penna et al. (2019). Initially, all the wells with available well-log data were used as hard constrains for the inversion. Then, we removed three wells to blind-tests and performed the inversion. The presented results in this publication are blind-test versions of the MCMC inversion.

The mean PI and DFU and MFU most probable occurrence from the 100 iterations, and the results of two random iterations are presented in Fig. 11. Clearly, one notices the relation and distribution of low-PI values as DFU3 and DFU4 and MFU5 to MFU8, while high-PI values tend to concentrate more DFU1 and DFU2 and, consequently, MFU1 to MFU4. Also, we noted how the occurrence of each MFU is conditioned to the occurrence of its correlated DFU. These sections are a good example of the advantage of using the seismic constraints over decametric scale and stochastic simulation over metric scale, below seismic resolution. To illustrate the special distribution, PI mean and DFU and MFU mode maps from the Itapema Formation are displayed in Fig. 12.

Overall, prior and posterior pdfs result for PI inversion are consistent, within few errors along Barra Velha and Itapema formations, except for MFU1 and MFU2 (Fig. 13). The reason for the discrepancy for these two flow units is the addition of an increasing a prior probability of DFU1 at lower structural regions (areas without drilled wells), mainly with predominance of mud sediments that corresponds to low PI values. Because of those areas, this pushes the posterior MFU1 and MFU2 PI values to the left of the plot. For the other MFUs, metrics such as mean, standard deviation, P10 and P90 are in match between prior and posterior pdfs.

The overall prior and posterior proportions of DFU and MFU for both Barra Velha and Itapema formations is presented in Fig. 14. MCMC inversion produced occurrence volumes that corroborate the well statistics. DFU, except for the wells used as blind-tests, are a perfect match between prior and posterior, because they were used as hard constraints at the well location. This is not the case for MFU, whose small deviations are observed between prior and posterior proportions.

5.4. Porosity and permeability cosimulation

We cosimulated for each PI iteration a numerous quantity of possible ϕ and permeability k volumes, given the MFU distributions calculated by the MCMC inversions. The procedure for the cosimulation is similarto the workflow described in Section 5.1, with the difference that the posterior probability is now coupled with the simulated PI value, there is, we are sampling for P(porosity|geostat, sim_{PI}) and P(permeability|geostat, sim_{PI}). It is important to emphasize that the porosity and permeability cosimulation is restricted with the MFU, below the seismic resolution. However, MFU is directly related to a specific DFU that is constrained by seismic data. So, at the end, the porosity and permeability are simulated on the metric scale without losing the seismic lateral control.

Through well data analysis and porosity and permeability volumes obtain from the Bayesian classification, the vertical and lateral experimental variograms are like those used to the PI MCMC inversion (Figs. 7 and 8). The porosity and permeability pdfs used for the cosimulation are showed in Fig. 15. As previously shown in Table 2 basic statistics, MFU1 concentrate worse permoporous samples and MFU8 better. We considered a cosimulation for each

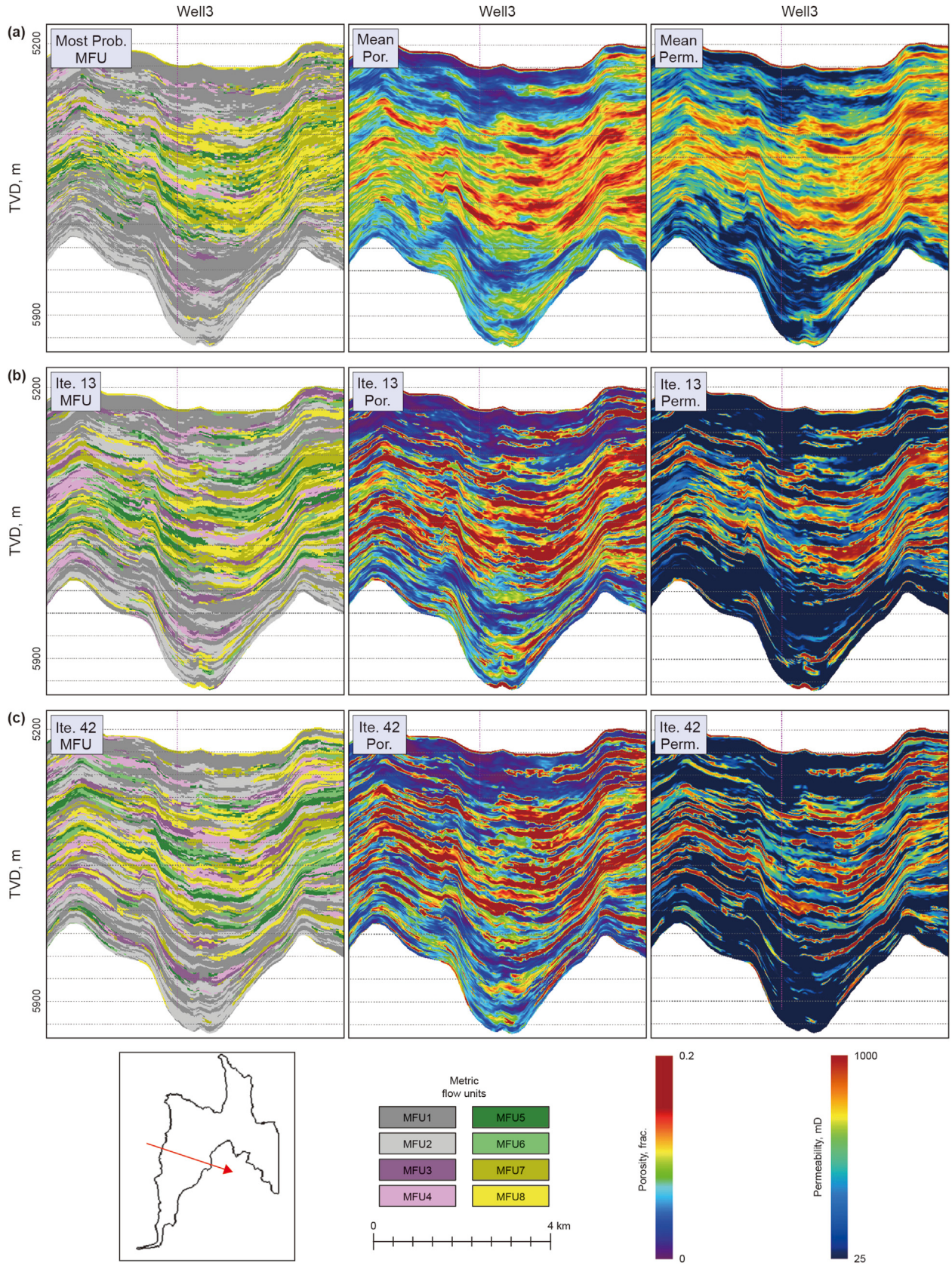

Fig. 16. **(a)** Most probable MFU and mean porosity and permeability NW-SE section from 100 cosimulation iterations. **(b)** Iteration 13 MFU, porosity and permeability results. **(c)** Iteration 42 MFU, porosity and permeability results.

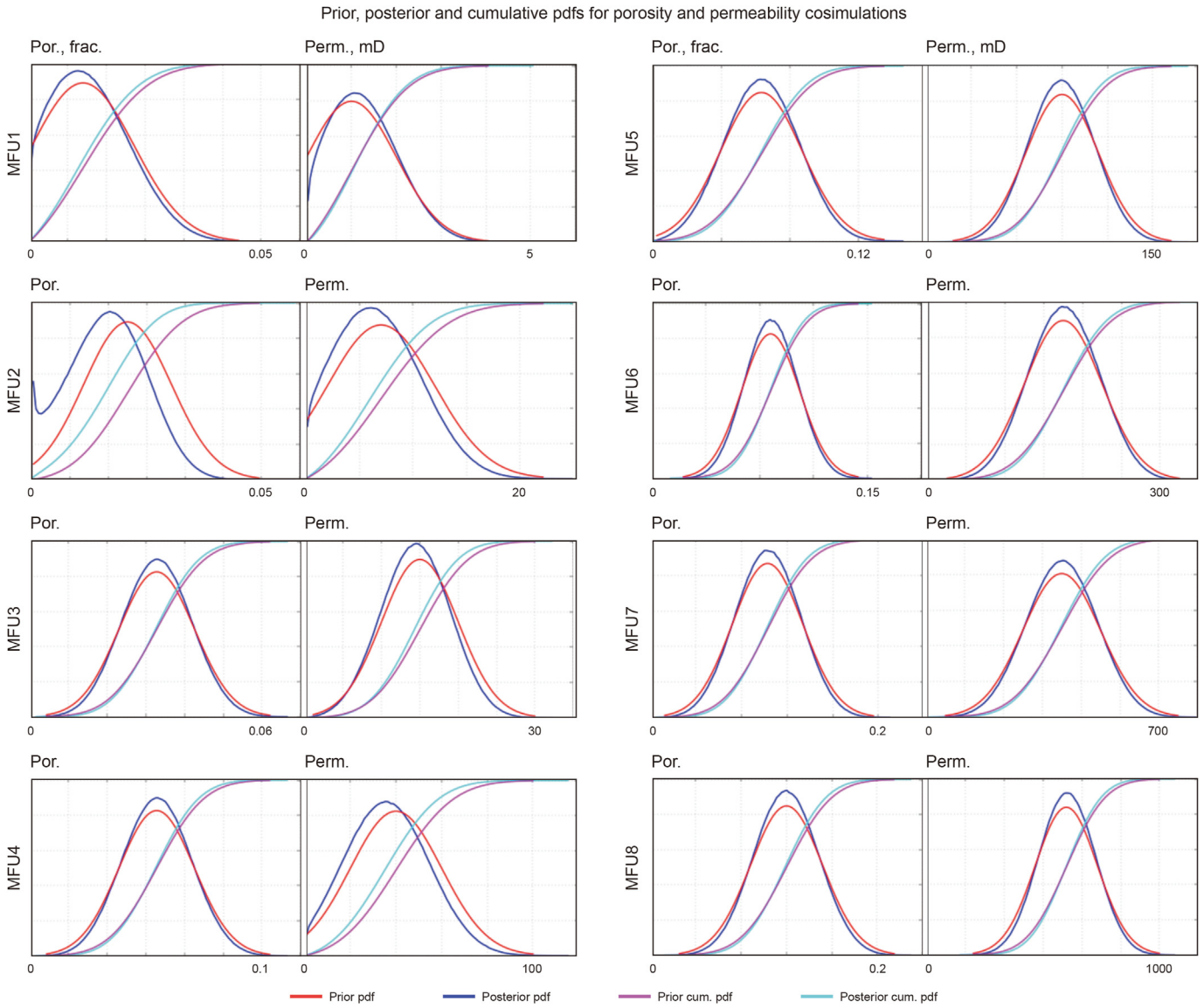

Fig. 17. Prior and posterior pdfs and cumulative pdfs for the 100 cosimulations for porosity and permeability.

MCMC iteration, that is, 100 possible porosity and permeability solutions were calculated given the input variograms, pdfs and PI volumes. Mean and individual results are displayed in Fig. 16, as well as the corresponding MFU from the related MCMC inversion. In practice, given these results, we can stablish pessimistic, optimistic and base scenarios for the Mero reservoir considering parameters such as net to gross, porous volumes, and volume in place.

We also performed the prior and posterior pdfs analysis for the permeability and porosity. As previously shown in the PI QC (Fig. 13), the cosimulation produces results below the seismic resolution that are compatible with the well data statistics, without relevant discrepancies and without losing the seismic constrain in the decametric scale. The pdf comparison is presented in Fig. 17. Also, in Fig. 18, inputs and mean outputs from porosity and permeability are displayed for two blind wells. Overall, the QC results corroborates the robustness and predictability of the method. A slighter higher amount of errors for MFU then DFU in the blind wells are expected, considering that the simulation constraint is stronger for decametric scale given the seismic vertical resolution characteristics. Thus, it's more reliable to analyze the posterior/prior pdfs analysis, once we are trying to mimic the probability distribution of the data. Summarizing, we produced a series of possible PI, DFU, MFU, porosity and permeability volumes through an MCMC inversion and cosimulation, which are laterally compatible with the seismic data and vertically with the well data statistics (Fig. 19).

6. Conclusions

The proposed workflow provided means to generate numerous

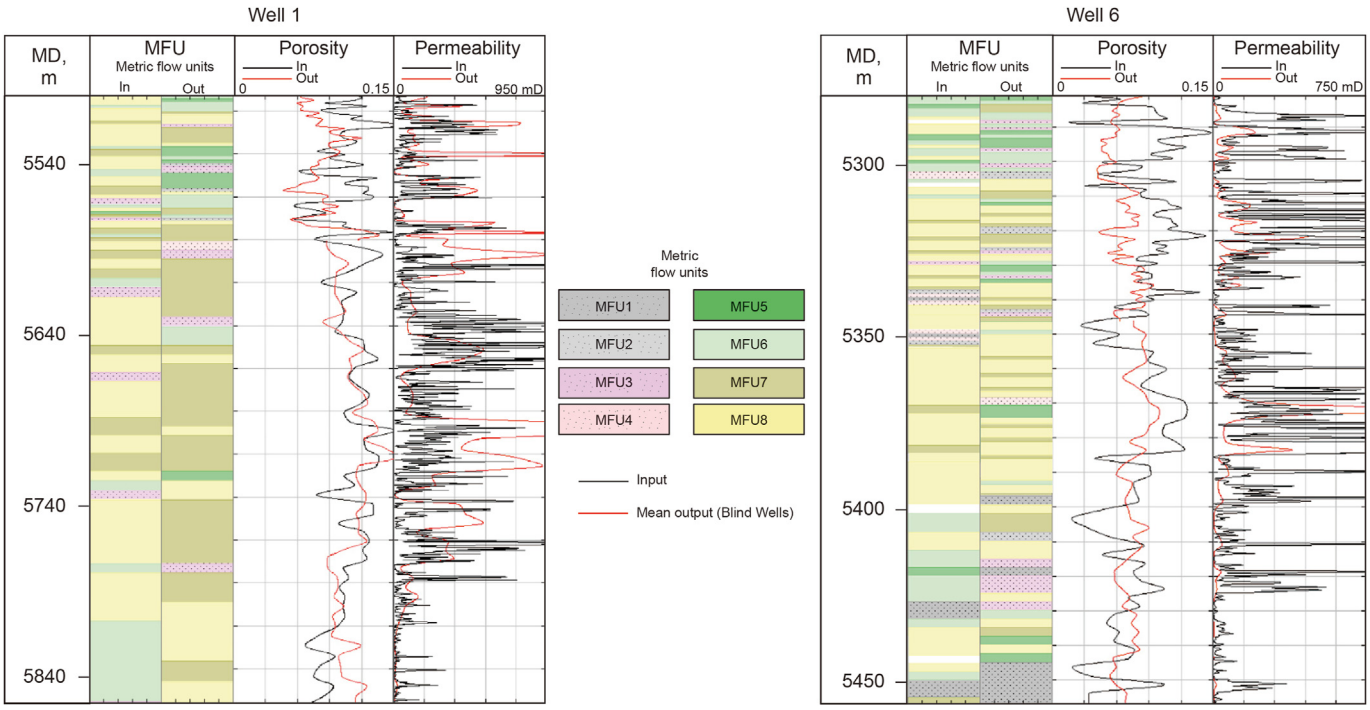

Fig. 18. MFU, porosity and permeability estimation QC for two blind wells in the area. Black lines correspond to input data and red lines to output data.

possible porosity and permeability 3D volumes below the seismic resolution limit, respecting the seismic data in decametric scale. Like many seismic Bayesian inference algorithms, the prior information plays an important role in the posterior distribution of PI and, consequently, porosity and permeability. We highly recommended that prior models are built representing local geology aspects or its analogs, constraining some characteristics that sometimes are not sampled even in the presence of numerous wells. That is the case of prior and posterior pdfs for MFU1 and MFU2, which the prior information volume forces the occurrence of worse permoporous facies (clay-rich carbonates) in structural lows, causing a deviation of posterior pdf towards low-PI values. These carbonates were not drilled by wells, once they are below the O/W contact. However, several analog data from other presalt reservoirs indicate the presence of such facies.

Even in the presence of high MFU superimposed zones in the acoustic domain, our workflow achieved a satisfactory posterior blind-well proportion. This issue can be addressed by generating a sufficient number of iterations and constraining MFU with its corresponding DFU, guaranteeing the seismic correlation at larger scales. As shown in previous studies, DFU presents a reduced amount of elastic and acoustic superimposition and can be quantified in terms of deterministic inversion and Bayesian probabilistic classification. However, the presence of noise and imaging problems in the seismic can propagate errors in the decametric scale to metric scale, causing porosity and permeability deviations.

Understanding flow behavior at decametric scale is the first step to build the dynamic reservoir knowledge at smaller scales, but detailed analysis can be performed with much more accuracy in the metric scale. In complex reservoir settings, where the fluid flow is inflected by numerous processes, it is important to have more flow units to correctly characterize the flow behavior, producing more accurate porosity and permeability relations and, consequently, a better volumetric distribution of these properties. Due to vertical resolution limitations, the distribution of MFU is not constrained by the seismic data, being dependent exclusively on the simulation method used. This can lead to some calculation errors that falls along any method of lateral extrapolation of discrete and continuous properties chosen. However, we tried to address this problem constraining the calculation of MFU with the occurrence of DFU. In this decametric scale the seismic can constrain the results, minimizing some of the large errors that could occur. We strongly recommend that some uncertainty analysis be performed through the probabilistic outputs of the workflow. We believe that interpretation of scenarios based on the volumes generated by the proposed methodology (e.g. P10, P50 and P90) will positively impact the static and dynamic model building process, as well as 4D seismic interpretation and seismic assisted history matching.

CRediT authorship contribution statement

Rodrigo Penna: Writing – review & editing, Writing – original draft, Methodology, Investigation, Formal analysis, Data curation, Conceptualization. **Wagner Moreira Lupinacci:** Validation, Supervision, Project administration.

Declaration of competing interest

The authors declare that they have no known competing financial interests or personal relationships that could have appeared to influence the work reported in this paper.

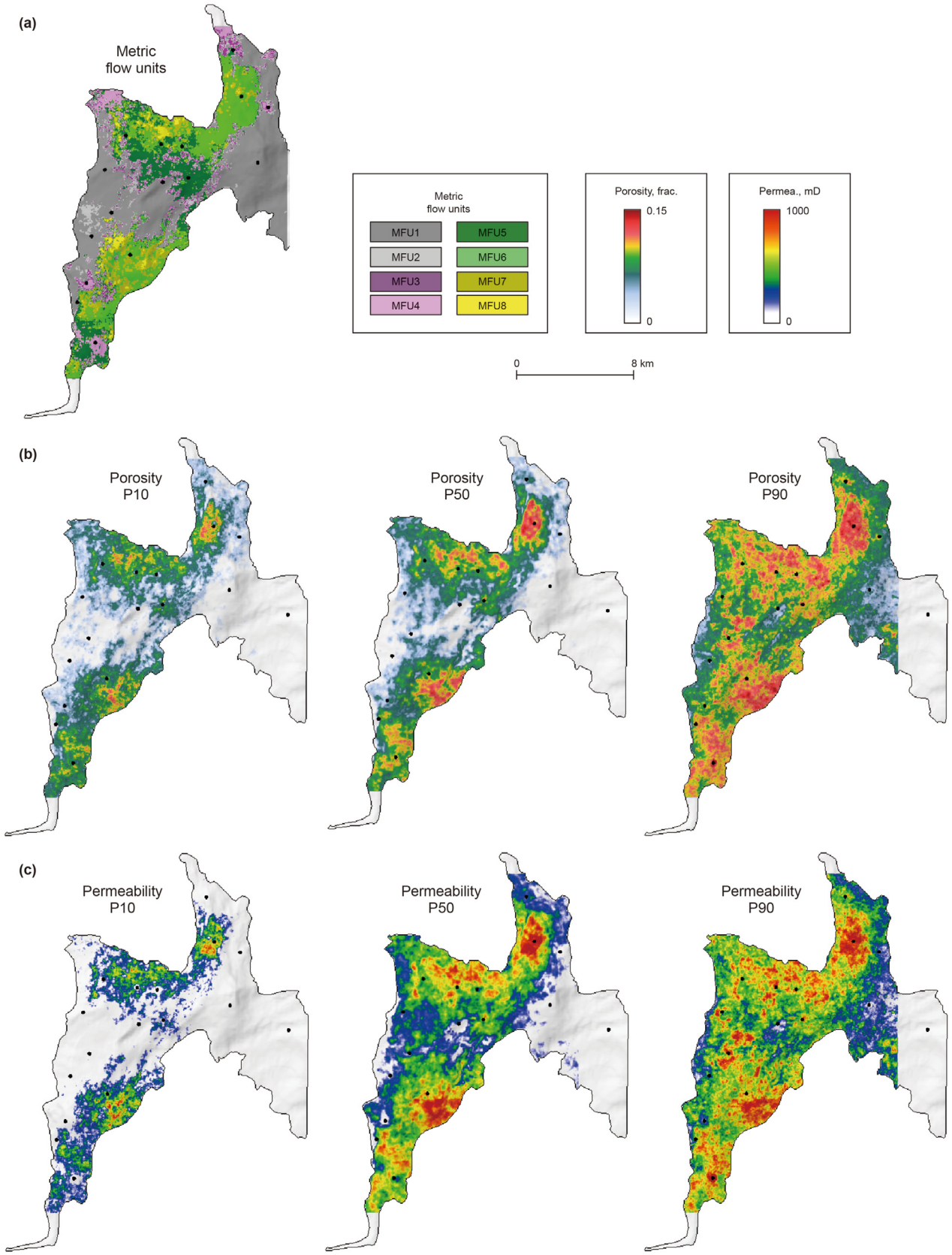

Fig. 19. **(a)** MFU mode map from the upper Barra Velha Formation. **(b)** Porosity and **(c)** permeability minimum, maximum and mean maps from the same stratigraphic layer.

Acknowledgements

The authors thank the Petrobras Libra JPT project and partners (Shell, Total, CNOOC and CNPC) for the data availability. We kindly appreciate Petrobras's Camilla Almeida, Marcos Sebastião, Vitor Mello, André Luis Souza, Rodolfo Victor, Antonio Carlos Nascimento, Leonardo Teixeira, Alexandre Maul and Shell's Louis Sturgess and Wences Gouveia for the technical support and discussions.

References

Al-Ajmi, F.A., Holditch, S.A., 2000. Permeability estimation using hydraulic flow units in a central arabia reservoir. In: SPE Annual Technical Conference and Exhibition. https://doi.org/10.2118/63254-ms.

Amaefule, J.O., Altunbay, M., Tiab, D., Kersey, D.G., Keelan, D.K., 1993. Enhanced reservoir description: using core and log data to identify hydraulic (flow) units and predict permeability in uncored intervals/wells. In: SPE Annual Technical Conference and Exhibition. https://doi.org/10.2118/26436-ms.

Araujo, S., Gouveia, W.P., 2015. Improved Presalt Imaging from Post-salt High-Resolution Velocity Updates. 14th International Congress of the Brazilian Geophysical Society & EXPOGEF, Rio de Janeiro, Brazil. https://doi.org/10.1190/sbgf2015-215, 3-6 August 2015.

Azevedo, L., Soares, A., 2018. Geostatistical methods for reservoir geophysics by Azevedo, L. and Soares, A. Math. Geosci. 50 (7), 861–863. https://doi.org/10.1007/s11004-018-9748-8.

Buckley, J.P., Bosence, D., Elders, C., 2015. Tectonic setting and stratigraphic architecture of an early cretaceous lacustrine carbonate platform, sugar loaf high, Santos Basin, Brazil. Geological Society, London, Special Publications 418 (1), 175–191. https://doi.org/10.1144/SP418.13.

Carlotto, M.A., da Silva, R.C.B., Yamato, A.A., Trindade, W.L., Moreira, J.L.P., Fernandes, R.A.R., Ribeiro, O.J.S., Gouveia, W.P., Carminati, J.P., Qicai, D., Junfeng, Z., da Silva-Telles, A.C., 2017. Libra: a newborn giant in the brazilian presalt province. In: In Giant Fields of the Decade 2000–2010. The American Association of Petroleum Geologists. https://doi.org/10.1306/13572006m1133685.

Deutsch, C.V., Journel, A.G., 1997. GSLIB Geostatistical Software Library andUser's Guide, second ed. Oxford University Press, New York.

Doyen, P., 2007. Seismic Reservoir Characterization: an Earth Modelling Perspective (EET 2). EAGE Publications bv. https://doi.org/10.3997/9789073781771.

Escobar, I., Williamson, P., Cherrett, A., Doyen, P.M., Bornard, R., Moyen, R., Crozat, T., 2006. Fast geostatistical stochastic inversion in a stratigraphic grid. In: SEG Technical Program Expanded Abstracts. https://doi.org/10.1190/1.2369943.

Feng, R., Luthi, S.M., Gisolf, D., 2018. Simulating reservoir lithologies by an actively conditioned Markov chain model. J. Geophys. Eng. 15 (3), 800–815. https://doi.org/10.1088/1742-2140/aaa0ff.

Ferreira, D.J.A., Lupinacci, W.M., 2018. An approach for three-dimensional quantitative carbonate reservoir characterization in the Pampo field, Campos Basin, offshore Brazil. Am. Assoc. Petrol. Geol. Bull. 102, 2267–2282. https://doi.org/10.1306/04121817352.

Ghanbarian, B., Lake, L.W., Sahimi, M., 2018. Insights into rock typing: a critical study. SPE J. 24 (1), 230–242. https://doi.org/10.2118/191366-pa.

Gomes, J.P., Bunevich, R.B., Tedeschi, L.R., Tucker, M.E., Whitaker, F.F., 2020. Facies classification and patterns of lacustrine carbonate deposition of the Barra Velha Formation, Santos Basin, Brazilian presalt. Mar. Petrol. Geol. 113, 104176. https://doi.org/10.1016/j.marpetgeo.2019.104176.

Gunter, G.W., Finneran, J.M., Hartmann, D.J., Miller, J.D., 1997. Early determination of reservoir flow units using an integrated petrophysical method. In: SPE Annual Technical Conference and Exhibition. https://doi.org/10.2118/38679-MS.

Haas, A., Dubrule, O., 1994. Geostatistical inversion—a sequential method of stochastic reservoir modelling constrained by seismic data. First Break 12 (11). https://doi.org/10.3997/1365-2397.1994034.

Haridy, M.G., Sedighi, F., Ghahri, P., Ussenova, K., Zhiyenkulov, M., 2020. Comprehensive study of the Oda corrected permeability upscaling method. In: Day 2 Wed, October 30, 2019. SPE/IATMI Asia Pacific Oil & Gas Conference and Exhibition. https://doi.org/10.2118/196399-MS.

Hatampour, A., Schaffie, M., Jafari, S., 2018. Hydraulic flow units' estimation from seismic data using artificial intelligence systems, an example from a gas reservoir in the Persian Gulf. J. Petrol. Sci. Eng. 170, 400–408. https://doi.org/10.1016/j.petrol.2018.06.086.

Herlinger Jr., R., Zambonato, E.E., De Ros, L.F., 2017. Influence of diagenesis on the quality of lower cretaceous presalt lacustrine carbonate reservoirs from Northern Campos Basin, Offshore Brazil. J. Sediment. Res. 87 (12), 1285–1313. https://doi.org/10.2110/jsr.2017.70.

Iravani, M., Rastegarnia, M., Javani, D., Sanati, A., Hajiabadi, S.H., 2018. Application of seismic attribute technique to estimate the 3d model of hydraulic flow units: a case study of a gas field in Iran. Egyptian Journal of Petroleum 27 (2), 145–157. https://doi.org/10.1016/j.ejpe.2017.02.003.

Jesus, C., Azul, M.O., Lupinacci, W., Machado, L., 2017. Mapping of carbonate mounds in the Brazilian presalt zone. In: SEG Technical Program Expanded Abstracts. https://doi.org/10.1190/segam2017-17789870.1, 2017.

Kneller, E., Teixeira, L., Hak, B., Cruz, N.M., Oliveira, T., Cruz, J.M., Cunha, R.S., 2019. Challenges and solutions of geostatistical inversion for reservoir characterization of the Supergiant Lula Field. Petroleum Geostatistics 1–5. https://doi.org/10.3997/2214-4609.201902176, 2019.

Kozeny, J., 1927. Ueber kapillare Leitung des Wassers im Boden. Sitzungsber Akad 136 (2a), 271–306.

Leite, C., de Assis Silva, C.M., de Ros, L.F., 2020. Depositional and diagenetic processes in the presalt rift section of a Santos Basin area, SE Brazil. J. Sediment. Res. 90 (6), 584–608. https://doi.org/10.2110/jsr.2020.27.

Li, P., Zheng, M., Bi, H., Wu, S., Wang, X., 2017. Pore throat structure and fractal characteristics of tight oil sandstone: a case study in the Ordos Basin, China. J. Petrol. Sci. Eng. 149, 665–674. https://doi.org/10.1016/j.petrol.2016.11.015.

Lima, B.E.M., De Ros, L.F., 2019. Deposition, diagenetic and hydrothermal processes in the Aptian Presalt lacustrine carbonate reservoirs of the northern Campos Basin, offshore Brazil. Sediment. Geol. 383, 55–81. https://doi.org/10.1016/j.sedgeo.2019.01.006.

Liu, Y., Liu, Y., Zhang, Q., Li, C., Feng, Y., Wang, Y., Xue, Y., Ma, H., 2019. Petrophysical static rock typing for carbonate reservoirs based on mercury injection capillary pressure curves using principal component analysis. J. Petrol. Sci. Eng. 181, 106175. https://doi.org/10.1016/j.petrol.2019.06.039.

Mahjour, S.K., Al-Askari, M.K.G., Masihi, M., 2016. Identification of flow units using methods of Testerman statistical zonation, flow zone index, and cluster analysis in Tabnaak gas field. J. Pet. Explor. Prod. Technol. 6 (4), 577–592. https://doi.org/10.1007/s13202-015-0224-4.

Mirzaei-Paiaman, A., Ostadhassan, M., Rezaee, R., Saboorian-Jooybari, H., Chen, Z., 2018. A new approach in petrophysical rock typing. J. Petrol. Sci. Eng. 166, 445–464. https://doi.org/10.1016/j.petrol.2018.03.075.

Moczydlower, B., Pacifico, F., Pizarro, J., 2019. Libra extended well test – an innovative approach to de-risk a complex field development. In: Presented at the Offshore Technology Conference. Houston, Texas, USA, 6-9 May 2019.

Moreira, J.L.P., Madeira, C.V., Gil, J.A., e Machado, M.A.P., 2007. Bacia de Santos. Bol. Geociencias Petrobras 15 (2), 531–549.

Nabawy, B.S., Basal, A.M.K., Sarhan, M.A., Safa, M.G., 2018. Reservoir zonation, rock typing and compartmentalization of the tortonian-serravallian sequence, temsah gas field, offshore nile delta, Egypt. Mar. Petrol. Geol. 92, 609–631. https://doi.org/10.1016/j.marpetgeo.2018.03.030.

Neves, I.A., Lupinacci, W.M., Ferreira, D.J.A., Zambrini, J.P.R., Oliveira, L.O.A., Olho Azul, M., Ferrari, A.L., Gamboa, L.A.P., 2019. Presalt reservoirs of the Santos Basin: cyclicity, electrofacies, and tectonic-sedimentary evolution. Interpretation 7, SH33–SH43. https://doi.org/10.1190/INT-2018-0237.1.

Oliveira, L., Rancan, C.C., Sartorato, A.C.L., Farias, F.A., Pereira, E., 2021. Drowning unconformities on presalt carbonate platforms – examples from the Itapema Formation (lower cretaceous), Santos Basin, offshore Brazil. In: Palaeogeography, Palaeoclimatology, Palaeoecology 577, 110570. https://doi.org/10.1016/j.palaeo.2021.110570.

Peçanha, A.A., Lupinacci, W.M., Ferreira, D.J.A., Freire, A.F.M., 2019. A workflow for reservoir characterization applied to presalt coquinas from the Linguado Field, Campos Basin, Brazil. J. Petrol. Sci. Eng. 183, 106451. https://doi.org/10.1016/j.petrol.2019.106451.

Penna, R., Araújo, S., Geisslinger, A., Sansonowski, R., Oliveira, L., Rosseto, J., Matos, M., 2019. Carbonate and igneous rock characterization through reprocessing, FWI imaging, and elastic inversion of a legacy seismic data set in Brazilian presalt province. Lead. Edge 38 (1), 11–19. https://doi.org/10.1190/tle38010011.1.

Penna, R., Lupinacci, W.M., 2020. Decameter-scale flow-unit classification in Brazilian presalt carbonates. SPE Reservoir Eval. Eng. 23 (4), 1420–1439. https://doi.org/10.2118/201235-pa.

Penna, R., Lupinacci, W.M., 2021. 3D modelling of flow units and petrophysical properties in Brazilian presalt carbonate. Mar. Petrol. Geol. 124, 104829. https://doi.org/10.1016/j.marpetgeo.2020.104829.

Pereira, Á., Nunes, R., Azevedo, L., Guerreiro, L., Soares, A., 2017. Geostatistical seismic inversion for frontier exploration. Interpretation 5 (4), T477–T485. https://doi.org/10.1190/int-2016-0171.1.

Rastegarnia, M., Sanati, A., Javani, D., 2016. A comparative study of 3D FZI and electrofacies modeling using seismic attribute analysis and neural network technique: a case study of Cheshmeh-Khosh Oil field in Iran. Petroleum 2 (3), 225–235. https://doi.org/10.1016/j.petlm.2016.06.005.

Rocha, H.O., da Costa, J.L.S., Carrasquilla, A.A.G., Carrasco, A.M.V., 2019. Petrophysical characterization using well log resistivity and rock grain specific surface area in a fractured carbonate presalt reservoir in the Santos Basin, Brazil. J. Petrol. Sci. Eng. 183, 106372. https://doi.org/10.1016/j.petrol.2019.106372.

Saussus, D., Sams, M., 2012. Facies as the key to using seismic inversion for modelling reservoir properties. First Break 30 (7). https://doi.org/10.3997/1365-2397.2012009.

Sams, M., Millar, I., Satriawan, W., Saussus, D., Bhattacharyya, S., 2011. Integration of geology and geophysics through geostatistical inversion: a case study. First Break 29 (8). https://doi.org/10.3997/1365-2397.2011023.

Sartorato, A.C.L., Tonietto, S.N., Pereira, E., 2020. Silicification and dissolution features in the brazilian Presalt Barra Velha formation: impacts in the reservoir quality and insights for 3D geological modeling. Rio Oil and Gas Expo and Conference 20, 68–69. https://doi.org/10.48072/2525-7579.rog.2020.068.

Seifert, I., Penna, R., Maul, A., González, M., 2017. Accurate Velocity Model Refinement through the Use of Acoustic Impedance for Evaporite Seismic Facies Differentiation of Presalt Reservoir Prospects in Santos Basin. 15th International Congress of the Brazilian Geophysical Society & EXPOGEF, Rio de Janeiro, Brazil. https://doi.org/10.1190/sbgf2017-351, 31 July-3 August 2017.

Soares, A., 2001. Direct sequential simulation and cosimulation. Math. Geol. 33 (8), 911–926. https://doi.org/10.1023/a:1012246006212.
Soares, A., Diet, J.D., Guerreiro, L., 2007. Stochastic inversion with a global perturbation method. In: EAGE Conference on Petroleum Geostatistics. EAGE Conference on Petroleum Geostatistics. https://doi.org/10.3997/2214-4609.201403048.
Tiab, D., Donaldson, E.C., 2004. Petrophysics: Theory and Practice of Measuring Reservoir Rock and Fluid Transport Properties. Gulf Professional Publishing.
Wheeler, H., 1958. Time-stratigraphy. AAPG (Am. Assoc. Pet. Geol.) Bull. 42 (5), 1047–1063. https://doi.org/10.1306/0bda5af2-16bd-11d7-8645000102c1865d.
Wright, V.P., Barnett, A.J., 2015. An abiotic model for the development of textures in some South Atlantic early Cretaceous lacustrine carbonates. Geological Society, London, Special Publications 418 (1), 209–219.
Yarmohammadi, S., Kadkhodaie-Ilkhchi, A., Rahimpour-Bonab, H., Shirzadi, A., 2014. Seismic reservoir characterization of a deep water sandstone reservoir using hydraulic and electrical flow units: a case study from the Shah Deniz gas field, the South Caspian Sea. J. Petrol. Sci. Eng. 118, 52–60. https://doi.org/10.1016/j.petrol.2014.04.002.
Zhang, P., Zhang, J., Wang, J., Li, M., Liang, J., Wu, Y., 2018. Flow units classification for geostatisitical three-dimensional modeling of a non-marine sandstone reservoir: a case study from the Paleocene Funing Formation of the Gaoji Oilfield, east China. Open Geosci. 10 (1), 113–120. https://doi.org/10.1515/geo-2018-0009.